PNAS

www.pnas.org

Supplementary Information for
Microstructural design for mechanical-optical multifunctionality in the exoskeleton of flower beetle *Torynorrhina flammea*

Zian Jia, Matheus C. Fernandes, Zhifei Deng, Ting Yang, Qiuting Zhang, Alfie Lethbridge, Jie Yin, Jae-Hwang Lee, Lin Han, James C. Weaver, Katia Bertoldi, Joanna Aizenberg, Mathias Kolle, Pete Vukusic, and Ling Li

Ling Li, Mathias Kolle, and Pete Vukusic
E-mail: lingl@vt.edu, mkolle@mit.edu, and P.Vukusic@exeter.ac.uk.

This PDF file includes:

> Supplementary Note 1: Optical Modeling
> Supplementary Note 2: Mechanical Modeling
> Supplementary Figures: Figs. S1-37
> SI References

Supplementary Information Text

Note 1: Optical Modeling

Optical Modeling of Light Diffraction: _Thorynorrhina flamea_ beetles have an intricate architecture of hierarchical micro- and nano-scale features in the top layers of their cuticles, responsible for the beetles' bright iridescent coloration. The structure consists of hexagonally arranged micro-scale pillars embedded within a multilayer morphology. The multilayer determines the structures' overall spectral reflectivity, while the micro-pillars modulate the angular distribution of the reflected light. A sketch of the structures with the relevant parameters used for optical modeling is shown in Fig. S27.

The reflected intensity as a function of color (wavelength), polar angle, and azimuthal angle for this structure can be modeled elegantly with wave optics (akin to considering coherent scattering from identical, spatially related diffracting apertures). Considering a single pillar and its surrounding multilayer as the structure's fundamental unit element, we first find the diffraction signature of this element and then calculate the scattering profile of an array of micro-pillars as the coherent superposition of their individual diffraction signatures.

The diffraction signature of a unit element: The unit cell has a cylindrical symmetry, which directly implies a circular symmetry of the spatial pattern of reflected light amplitude. This ultimately leads to a circular symmetry in the angular distribution of the intensity of reflected light. The unit cell's radial variation of reflected light amplitude for two different wavelengths for a multilayer with a peak wavelength of 645 nm (which corresponds to the orange-red beetle in the main manuscript) is shown in Fig. S28.

The following calculations are done for normal incidence of light onto the beetle's micropillar-laced multilayer structure but can also be extended (with some additional mathematical complexity) to inclined incidence angles. The spatial distribution of reflected field amplitude (in general a complex number accounting for variations in phase) is given by

$$g(R) = \left(r_{\mathrm{p}} - r_{\mathrm{ml}}\right) \cdot \mathrm{circ}\left(\frac{R}{R_{\mathrm{p}}}\right) + r_{\mathrm{ml}}, \tag{1}$$

where R is the radial coordinate, R_{p} the pillar radius, r_{p} and r_{ml} the complex reflection coefficients of the micro-pillars and the multilayer. Here, the time dependency is omitted as it would just represent a constant phase term across the whole structure for any given point in time. The far-field amplitude distribution of the scattering structure can be described by a Fourier transform, which in spherical coordinates as a function of polar and azimuthal angles has the form

$$G(\theta, \varphi) = \int_0^\infty \int_0^{2\pi} g(R) \cdot e^{-2\pi i \frac{\sin\theta}{\lambda} R \cos(\varphi - \psi)} \, R \, d\psi \, dR,$$

where the integration is over radius R and azimuthal angle ψ. Using the identity of the Bessel function of first kind and zeroth order J_0 this can be rewritten as

$$G(\theta, \varphi) = 2\pi \int_0^\infty g(R) \cdot R \cdot J_0\left(2\pi \frac{\sin\theta}{\lambda} R\right) dR . \tag{2}$$

The coherence length of sunlight is around 20 μm (reference (1), p. 576). This means that a fair approximation to the integral is to limit the integration over the radius variable to a range of [-10μm, 10μm]. Using the variable $R_c = 10$ μm and substituting the expression from eq.1 into eq.2 gives,

$$G(\theta, \varphi) = 2\pi \int_0^{R_{\mathrm{p}}} \left(r_{\mathrm{p}} - r_{\mathrm{ml}}\right) \cdot R \cdot J_0\left(2\pi \frac{\sin\theta}{\lambda} R\right) dR + 2\pi \int_0^{R_c} r_{\mathrm{ml}} \cdot R \cdot J_0\left(2\pi \frac{\sin\theta}{\lambda} R\right) dR.$$

Using a change of variables $R' = 2\pi \frac{\cos\theta}{\lambda} R$ and $\int_0^k k' J_0(k') = k J_1(k)$, with $J_1(k)$ being the Bessel function of first kind and first order, this turns into

$$G(\theta, \varphi) = 2\pi R_{\mathrm{p}}^2 \cdot \left(r_{\mathrm{p}} - r_{\mathrm{ml}}\right) \cdot \frac{J_1\left(2\pi \frac{\sin\theta}{\lambda} R_{\mathrm{p}}\right)}{2\pi \frac{\sin\theta}{\lambda} R_{\mathrm{p}}} + 2\pi R_c^2 \cdot r_{\mathrm{ml}} \cdot \frac{J_1\left(2\pi \frac{\sin\theta}{\lambda} R_c\right)}{2\pi \frac{\sin\theta}{\lambda} R_c}. \tag{3}$$

The diffraction signature of a beetle's unit cell pillar-multilayer morphology is shown in Supplementary Fig. 28, which displays field density and phase, as well as the radiant intensity and angle-dependent color resulting from the calculation of $G(\theta, \varphi)$.

The diffraction of a hexagonally packed array of unit elements: With the diffraction signature $G(\theta, \varphi)$ of a unit element known, the diffracted light field of a periodic arrangement of unit cells $G_{\text{array}}(\theta, \varphi)$ can be calculated by coherent addition (see reference (1), p.444). The centers of each unit cell are given by $\vec{c}_{n,m} = m \cdot \begin{pmatrix} 1 \\ 0 \end{pmatrix} + n \cdot \begin{pmatrix} 1/2 \\ \sqrt{3}/2 \end{pmatrix}$ with $n, m \in \mathbf{Z}$. The coherence area of sunlight has a diameter of around 20 µm, as stated earlier. That means only unit cells within a coherence area of radius $R_c = 10$ µm need to be added coherently to obtain the overall diffraction signature of the beetles' cuticle architectures. For a pillar-to-pillar distance L this restricts the counters m, n to $|m| \leq \left\lfloor \frac{R_c}{L} \right\rfloor$ and $-\frac{m}{2} - \sqrt{\left\lfloor \frac{R_c}{L} \right\rfloor^2 - \frac{3}{4} m^2} \leq n \leq -\frac{m}{2} + \sqrt{\left\lfloor \frac{R_c}{L} \right\rfloor^2 - \frac{3}{4} m^2}$. $G_{\text{array}}(\theta, \varphi)$ can be expressed as

$$G_{\text{array}}(\theta, \varphi) = G(\theta, \varphi) \cdot \sum_{m,n} e^{-2\pi i \frac{\sin\theta}{\lambda} L \cdot \binom{\cos\varphi}{\sin\varphi} \cdot \vec{c}_{n,m}} \tag{4}$$

$$= G(\theta, \varphi) \cdot \sum_{m,n} e^{-2\pi i \frac{\sin\theta}{\lambda} L \cdot \left(m\cos\varphi + \frac{1}{2n}(\cos\varphi + \sqrt{3}\sin\varphi) \right)}.$$

The area over which the summation in eq.4 is done is bound by the coherence area of sunlight with a radius $R_c = 10$ µm (Fig. S29a). Features in the coherent reflection of light from the multilayer with periodic interruptions through micro-pillars are considerably sharper compared to the diffraction signature of a single unit cell. Most intensity is localized in the specular reflection direction, i.e., $\theta \approx 0°$ for normal light incidence (Fig. S30a,b).Fig. S31 shows the angular reflection characteristics of hexagonally arranged micro-pillars embedded within multilayers for the geometrical parameters of five different beetles.

One question that can be asked is how the beetles' cuticle structures compare to theoretically predicted structures that maximize the intensity in the first diffraction orders (i.e., at a polar angle of $\theta = \sin^{-1}(\lambda/L)$). Modeling the diffraction of multilayer-pillar structures with reflection spectra corresponding in peak reflection wavelength to the beetles' measured multilayer reflection signatures reveals that the beetles' pillar radii and distances are located very close to the optimum values predicted by the model (Fig. S32).

Note 2: Mechanical Modeling

The effective modulus of the beetle's bilayer structure is calculated based on a hexagonal pillar unit cell array. To obtain a theoretical approximate solution, we decompose this problem into a multilayer structure (Fig. S33) based on reference (2), pgs. 8-11 and use the rule of mixtures to account for the reinforcement effect contributed by the micro-pillars. We primarily focus on mechanical stiffness along the perpendicular loading direction, namely, the vertical e_3 direction in Fig. S33. The multilayer medium consists of a set of uniform infinite lamina, with alternating properties, bonded together across interfaces. Suppose that Young's moduli (E) and Poisson's ratios (v) are different for each individual material as depicted in Fig. S33. Furthermore, suppose that the volume fractions for each of the layers are c_1 and c_2, where $c_1 + c_2 = 1$.

Assuming both materials in the laminate are isotropic and there exist no interfacial effects between surfaces, we can develop a closed-form analytical solution for an infinite composite of such a structure. We begin by recalling the stress-strain relation for an isotropic material,

$$E\epsilon_{ij} = (1+v)\sigma_{ij} - v\delta_{ij}\sigma_{kk}. \tag{5}$$

where σ_{ij} and ϵ_{ij} are the stress and strain tensor, respectively, δ_{ij} is the Kronecker delta.

Thus, the transverse isotropy stress-strain relations can be given in the form,

$$E_1\epsilon_{11} = \sigma_{11} - v_{12}\sigma_{22} - v_{13}\sigma_{33}$$

$$E_1\epsilon_{22} = \sigma_{22} - v_{12}\sigma_{11} - v_{13}\sigma_{33}$$

$$E_1\epsilon_{12} = (1+v_{12})\sigma_{12}$$

$$E_3\epsilon_{33} = \sigma_{33} - v_{31}(\sigma_{11} + \sigma_{22})$$

$$2G_{13}\epsilon_{13} = \sigma_{13}, 2G_{13}\epsilon_{23} = \sigma_{23}$$

with interrelation $\frac{v_{13}}{E_1} = \frac{v_{31}}{E_3}$. Now, the first effective modulus E_3^{eff} can be obtained by imposing an effective stress in the parallel direction given as $\sigma_{33} = \bar{\sigma}_{33}$ throughout the composite. Thus, it is possible to find a field such that the strains in the lamina become constant, namely $\epsilon_{11} = \epsilon_{22} = \bar{\epsilon}_{11}$. The value of $\bar{\epsilon}_{11}$ is fixed by the requirement that the mean value of the stress component σ_{11} must be zero. Now, we can look at each lamina individually and obtain the governing equations such that:

$$E\epsilon_{33} = \bar{\sigma}_{33} - 2v\sigma_{11} \tag{6}$$

$$E\bar{\epsilon}_{11} = (1-v)\sigma_{11} - v\bar{\sigma}_{33} \tag{7}$$

Re-arranging eq. (7) we can get the uniaxial stress as

$$\sigma_{11} = \frac{E}{1-v}\bar{\epsilon}_{11} + \frac{v}{1-v}\bar{\sigma}_{33}. \tag{8}$$

Thus, if we require that the mean value of the stress of σ_{11} to be zero, we obtain the average formulation for the strain as (based on linear superposition of the stresses)

$$\bar{\epsilon}_{11} = -\left\langle\frac{E}{1-v}\right\rangle^{-1}\left\langle\frac{v}{1-v}\right\rangle\bar{\sigma}_{33}, \tag{9}$$

where the average is given in terms of the volume fractions $\langle\phi\rangle = c_1\phi_1 + c_2\phi_2 = f\phi_1 + (1-f)\phi_2$, given $f = c_1$ and $1 - f = c_2$. If we compare the transverse stress-strain relation to eq. (5), we can see that,

$$\frac{v_{13}^{\text{eff}}}{E_1^{\text{eff}}} = \left\langle\frac{E}{1-v}\right\rangle^{-1}\left\langle\frac{v}{1-v}\right\rangle = \frac{v_{31}^{\text{eff}}}{E_3^{\text{eff}}}.$$

Now, if we substitute eq. (9) into eq. (8) together with eq. (6), we obtain the expression for the strain:

$$\epsilon_{33} = \left\{\frac{(1-2v)(1+v)}{E(1-v)} + \frac{2v}{1-v}\left\langle\frac{E}{1-v}\right\rangle^{-1}\left\langle\frac{v}{1-v}\right\rangle\right\}\bar{\sigma}_{33} \tag{10}$$

The average of this equation gives, by definition, $\sigma_{33}^{\text{eff}}/E_3^{\text{eff}}$. Thus,

$$E_3^{\text{eff}} = \left|\frac{(1-2v)(1+v)}{E(1-v)} + \frac{2v}{1-v}\left\langle\frac{E}{1-v}\right\rangle^{-1}\left\langle\frac{v}{1-v}\right\rangle\right|^{-1}. \tag{11}$$

which can be rewritten as,

4

$$k_1 = \left(\frac{f_{ml}E_1}{1 - \nu_1} + \frac{(1 - f_{ml})E_2}{1 - \nu_2} \right)^{-1}$$

$$k_2 = \frac{f_{ml}\nu_1}{1 - \nu_1} + \frac{(1 - f_{ml})\nu_2}{1 - \nu_2}$$

$$E_{ml} = E_3^{eff} = \left(\frac{f_{ml}(1 - 2\nu_1)(1 + \nu_1)}{E_1(1 - \nu_1)} + \frac{(1 - f_{ml})(1 - 2\nu_2)(1 + \nu_2)}{E_2(1 - \nu_2)} + \frac{2f_{ml}\nu_1 k_1 k_2}{1 - \nu_1} \right.$$
$$\left. + \frac{2(1 - f_{ml})\nu_2 k_1 k_2}{1 - \nu_2} \right)^{-1}$$

with the multilayer volume fraction of material phase 1 described by $f_{ml} = \frac{L_1}{L_1 + L_2} = c_1$.

In the above formula, ν_1, E_1, L_1 are the properties of the layers with material 1 and ν_2, E_2, L_2 are properties of the layer with material 2.

Using the above as the solution for the stiffness of the bilayer matrix, we analyze the total composite by treating the bilayer as a homogeneous material. Thus, we use the rule of mixtures to obtain a total solution for the composite including the vertical micro-pillars and the bilayers as:

$$E_{Beetle}^{eff} = f_{pill}E_{pill} + \left(1 - f_{pill}\right)E_{ml}$$

$$f_{pill} = \frac{A_{mp}}{A_{ml} + A_{mp}}$$

where, A_{mp} is the cross-sectional area of all micro-pillars, and A_{ml} is the cross-sectional area normal to the load subtracting the area of the pillar ($A_{ml} = 1 - A_{mp}$). This solution assumes that there are no interfacial and bonding effects between the micro-pillars and the multilayer substrate. The dependency of the effective modulus of the pillar reinforced bilayer structure on the relative pillar radius is shown in Fig. S34.

To study the effects of the pillar distance and radius on the effective stiffness, we have selected a beetle, namely the red colored beetle, and used its material properties to analyze how the effective stiffness varies with pillar parameters. As Fig. S35 suggests, the stiffness of the beetle is more sensitive to the pillar radius than to the distance. Furthermore, if the relative volume fraction of bilayer material to the pillar is kept constant, the effective stiffness will also remain constant. It can be clearly seen that the more pillar mass is contained in the structure, the stiffer it becomes.
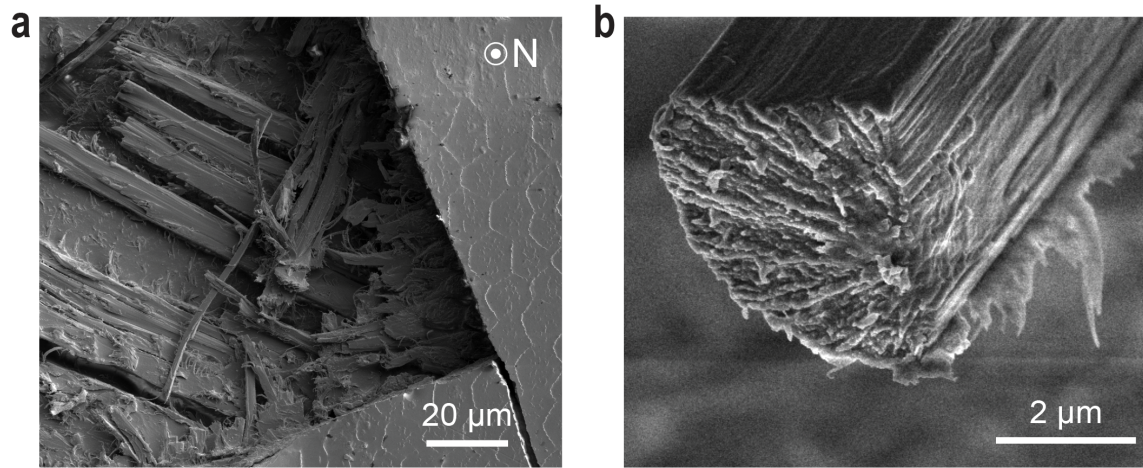
Supplementary Figures

Fig. S1 | Fibrous structure in the endocuticle region. **a**, A top-viewed SEM image of the fractured cuticle, showing the plywood-like structure in the endocuticle layer. **b**, Fractured cross-section of individual fibers in the endocuticle layer.
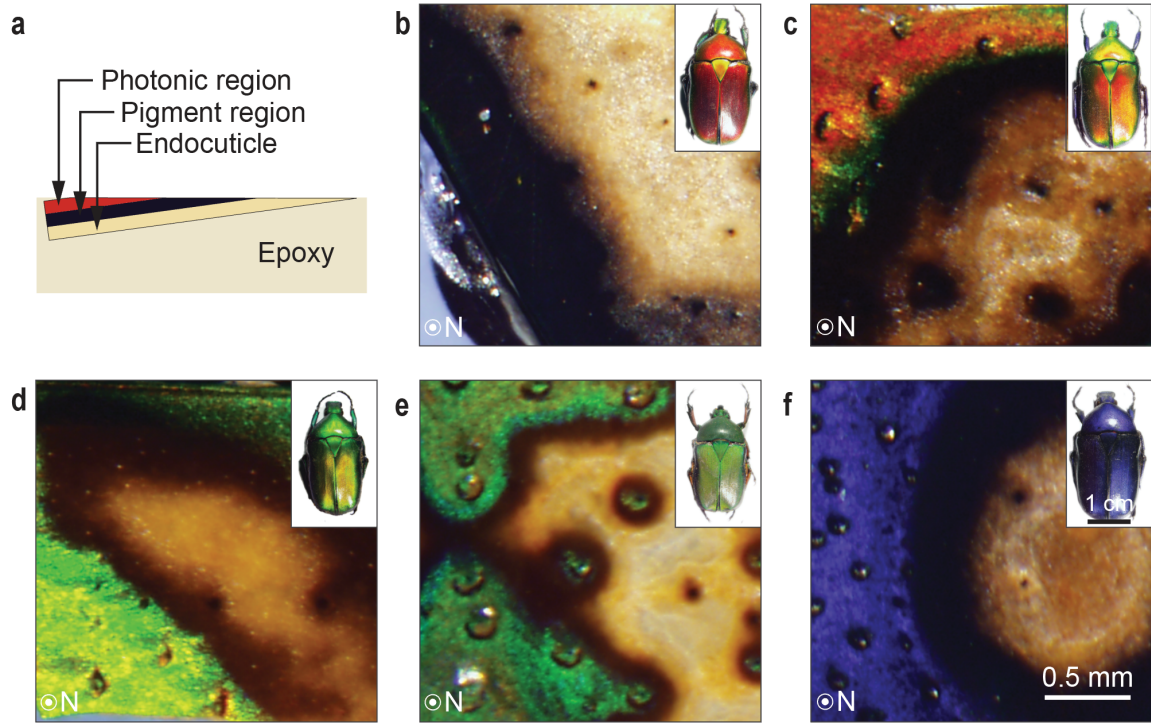
Fig. S2 | Subsurface microstructure analysis based on optica images from in-plane polishing. **a**, Schematic diagram of specimen orientation used for in-plane polishing. A square-shaped piece of cuticle cut from the elytra was placed in the horizontal orientation, subsequently placed at the bottom of the container, and embedded with epoxy. Due to the presence of natural surface curvature, a slight incline between the cuticle surface and the sample surface in some regions led to the exposure of underlying structures in the polishing. **b-f**, Representative optical images for beetle samples with the color of **b** red, **c** orange, **d** yellow-green, **e** green, and **f** purple. The inset pictures show the corresponding beetle samples.
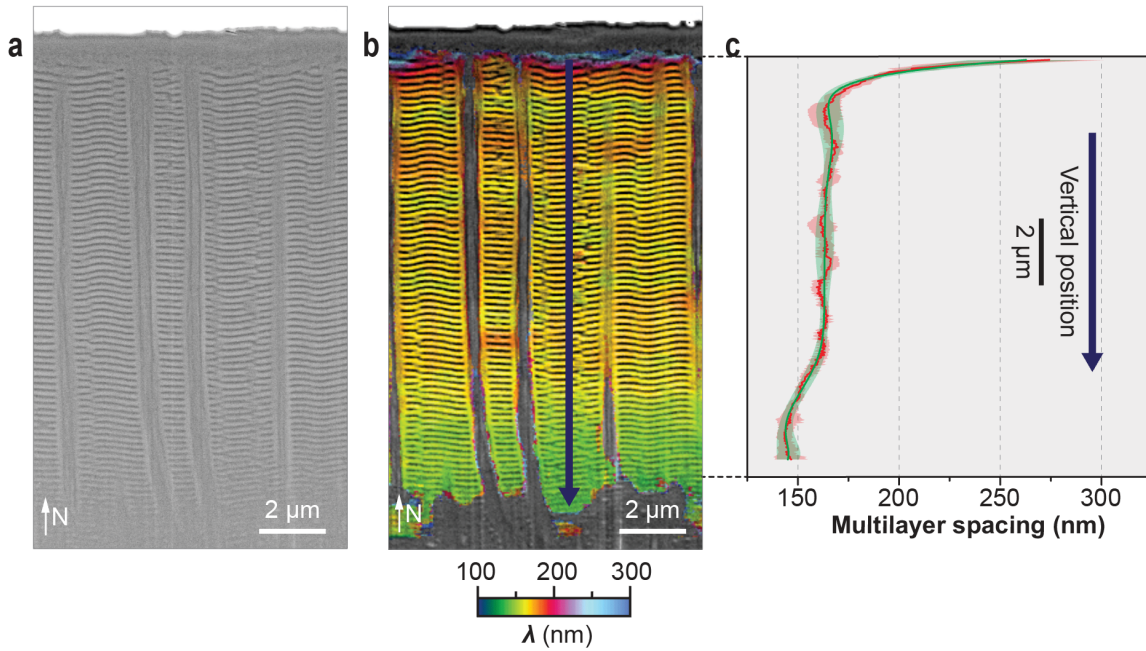
Fig. S3 | Variation of multilayer spacing in the photonic region. a, An SEM image of a vertical cross-section of the micropillar-nanomultilayer photonic structure in the beetle's exocuticle after FIB milling. **b**, Color map of the multilayer spacing. **c**, Multilayer spacing profile plotted as a function of vertical position from the surface of the cuticle.
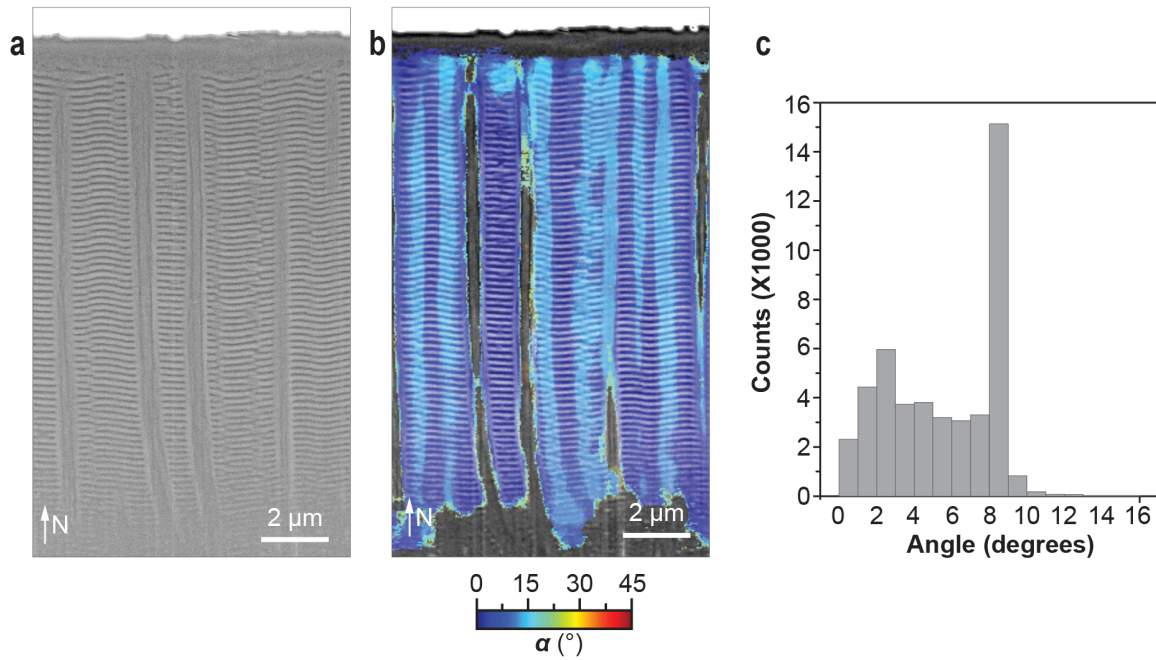
Fig. S4 | Variation of multilayer orientation in the photonic region. a, An SEM image of a vertical cross-section of the micropillar-nanomultilayer photonic structure in the beetle's exocuticle after FIB milling. **b**, The corresponding color map of orientation. **c**, Histogram of the multilayer orientation. Average ± standard deviation: 5.6 ± 2.9°.
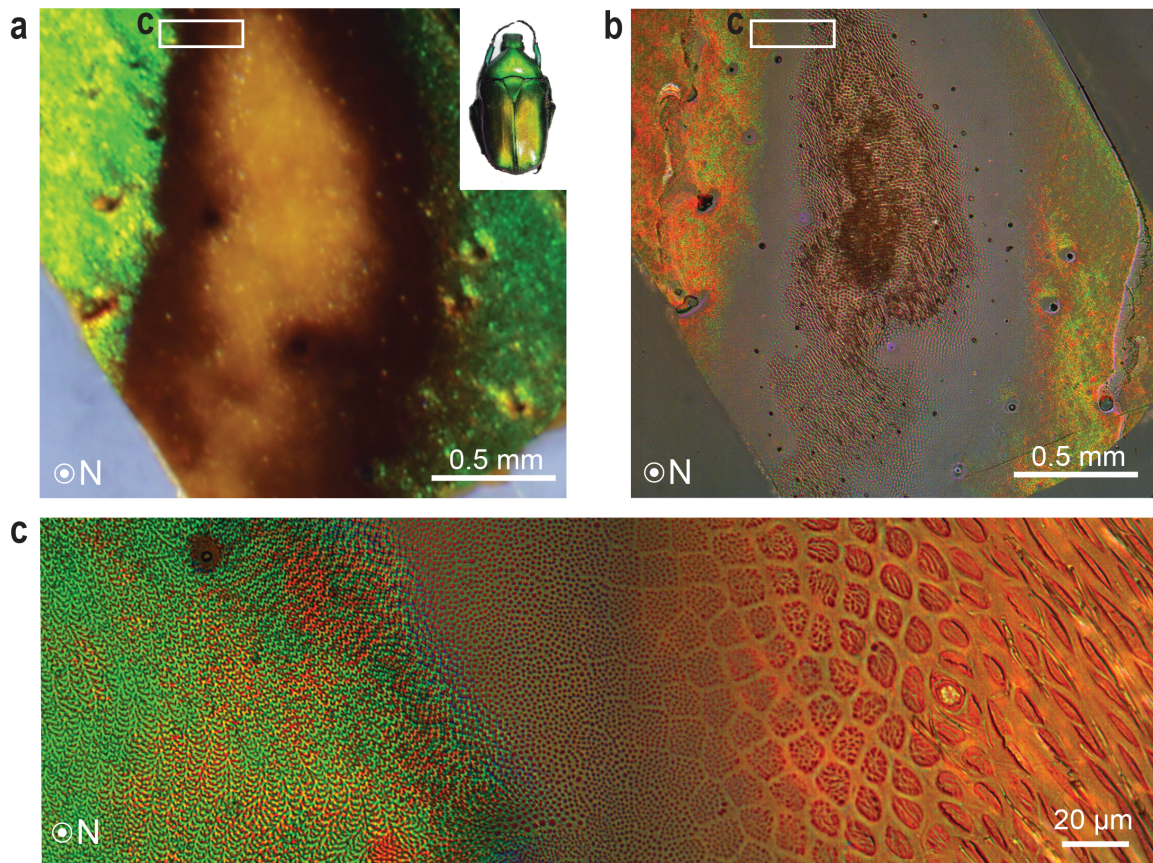
Fig. S5 | Morphological changes of the micropillars along the thickness direction in the beetle's cuticle. **a**, A photograph of an in-plane polished cuticle from a yellow-green *T. flammea* beetle. **b**, Image acquired with a reflection microscope in the same region. The white boxes in **a** and **b** indicate the location where the optical image in **c** was taken. **c**, A high-magnification optical image of the in-plane polished surface, illustrating the gradual transition from the photonic region to the underlying non-photonic pillar regions, which are gradually grouped to form fibers of larger-diameters.
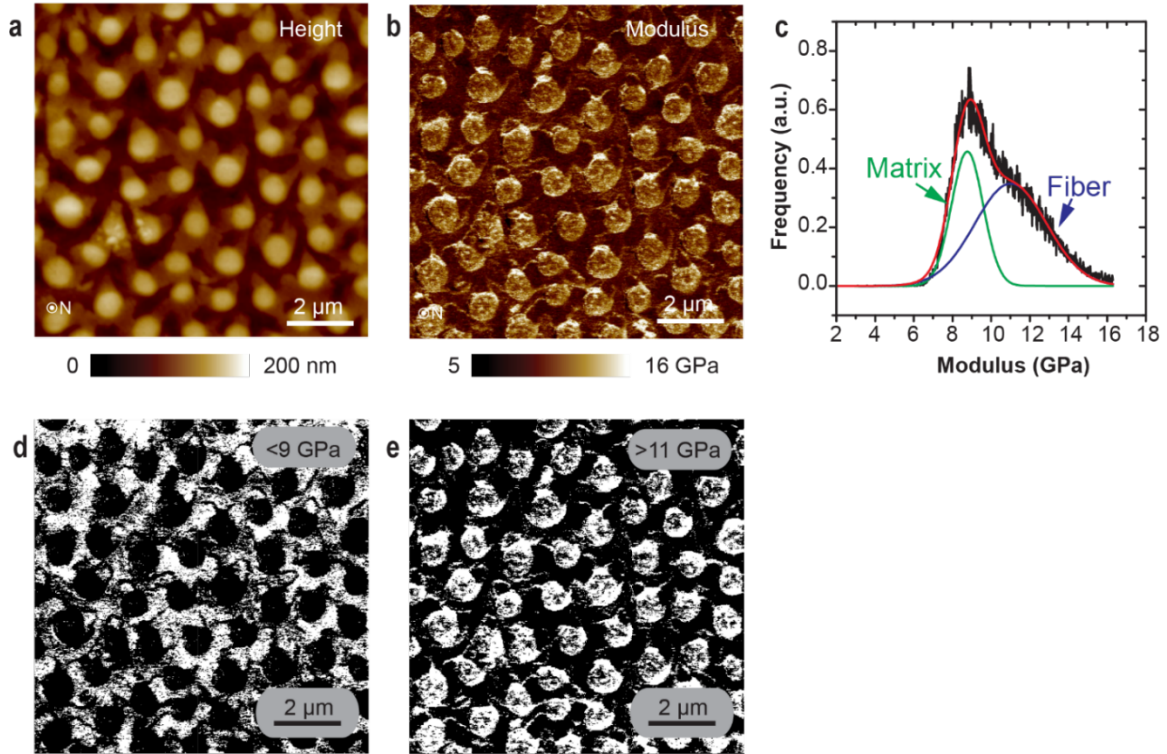
Fig. S6 | Quantitative nanomechanical mapping based on AFM measurements. a, AFM height image acquired on an in-plane polished specimen, revealing the individual vertical micro-pillars. **b**, Corresponding modulus mapping in the same region as **a**. **c**, Statistical distribution of modulus based on the modulus map shown in **b**. Two primary peaks can be identified for the "micro-pillars" and the "matrix". The corresponding averaged elastic modulus for these two phases are 11.0 GPa and 8.8 GPa, respectively. **d**, **e**, Binarized modulus maps with white color showing the regions of **d** modulus smaller than 9 GPa and **e** modulus greater than 11 GPa, respectively. The locations of the matrix and micro-pillars can be clearly identified in the binary images.
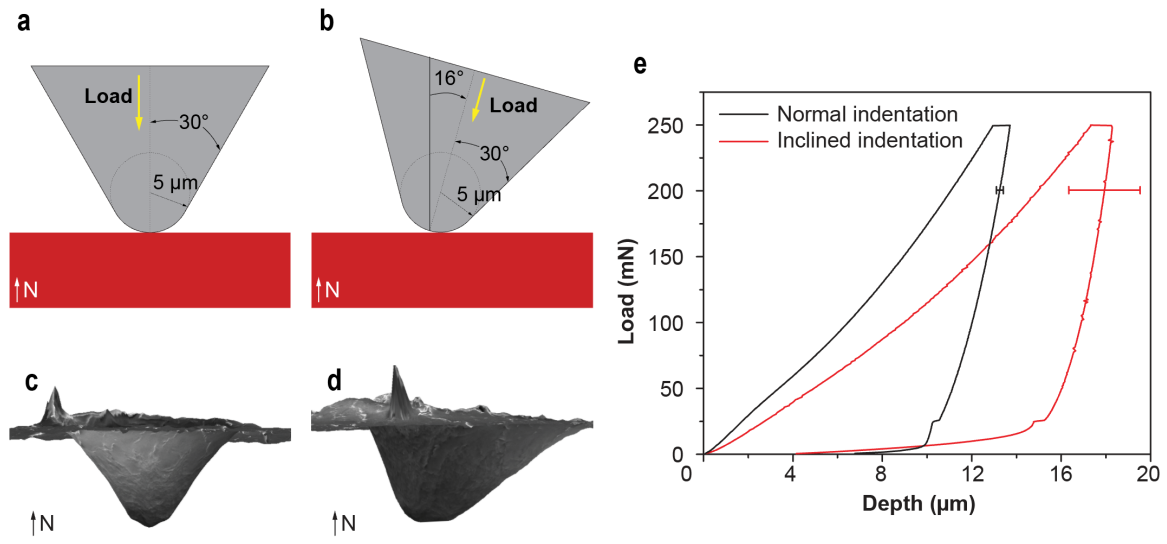
Fig. S7 | Schematic diagrams of micro-indentation on the beetle cuticle in **a** normal and **b** inclined directions. The indentation probe is a conospherical tip with a half angle of 30° and a tip radius of 5 μm. The inclination angle for the inclined indentation is 16°. Side view of the indentation residues for **c** normal and **d** inclined indentations based on stereological reconstruction from SEM images taken at two different tilt angles. **e**, Averaged force-depth curves for micro-indentations in both normal (n = 6) and inclined (n = 6) directions. The error bars indicate one standard deviation in displacement at 80% of maximum force.
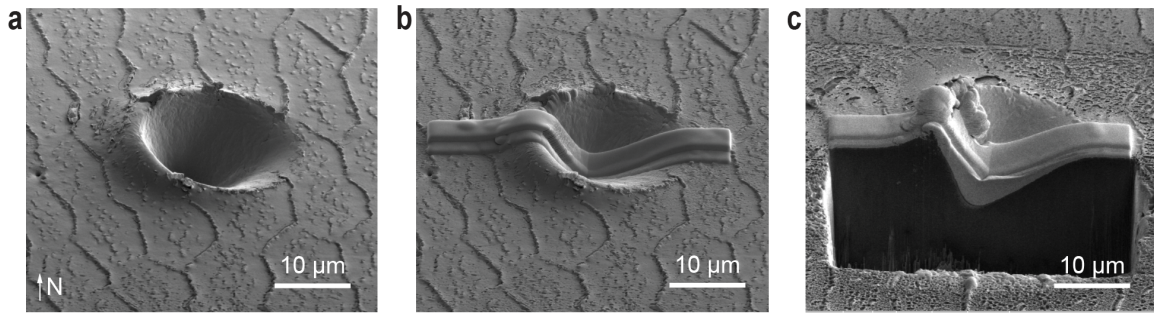
Fig. S8 | Experimental procedure for acquiring the cross-sectional images of the cuticle after micro-indentation tests. a, Original structure after inclined micro-indentation. **b**, The indentation crater was covered with a stripe of platinum protection layer. **c**, The underlying structure was revealed with FIB milling.
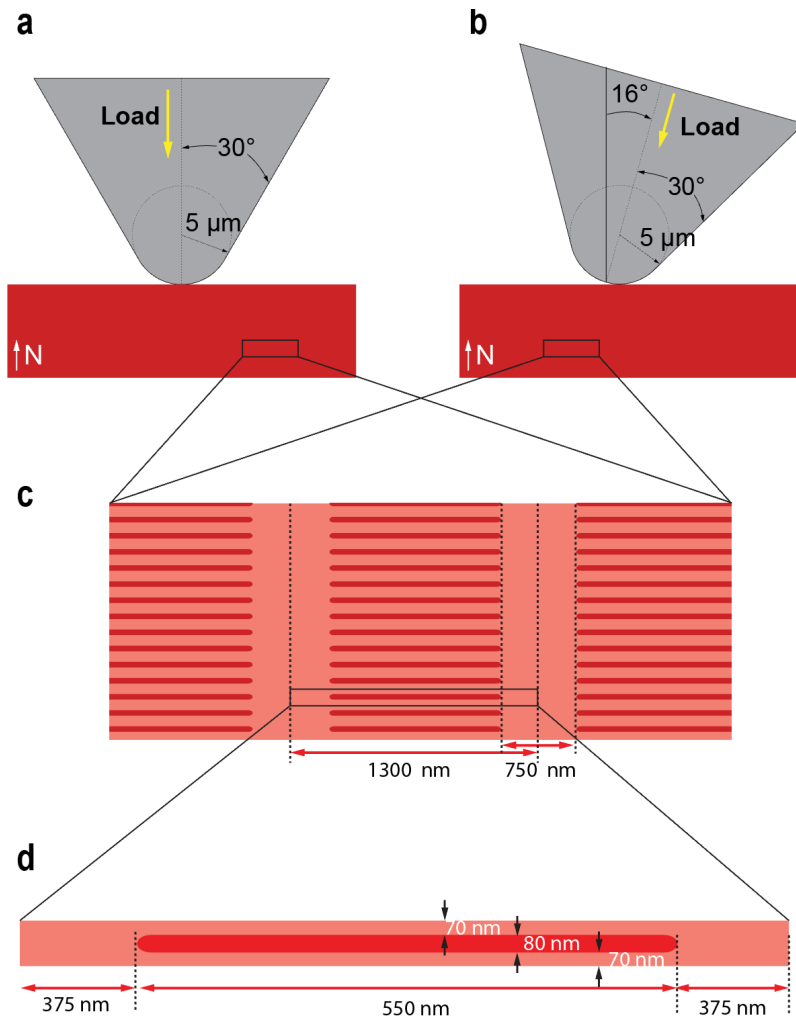
Fig. S9 | Summary of the mechanical finite element simulation setup. **a,b,** Schematic diagrams of the indenter geometry and indentation orientations. **c,d,** Schematic diagram of the cuticle composite used in the simulation. The dimensions of the multilayer and micropillars are based on experimental measurements of the red-colored *T. flammea* beetle.

Fig. S10 | FEM simulation results: normal indentation at maximum load. Three columns from left to right represent stress and strain distribution of the pillar-multilayer structure, multilayer structure, and a homogeneous material composed of the stiffer phase, respectively. Top to bottom rows represent structure, Mises stress, plastic strain (ε_p), normal stress (σ_{11} and σ_{22}), shear stress (σ_{12}), normal strain (ε_{11} and ε_{22}), and shear strain (ε_{12}), respectively.
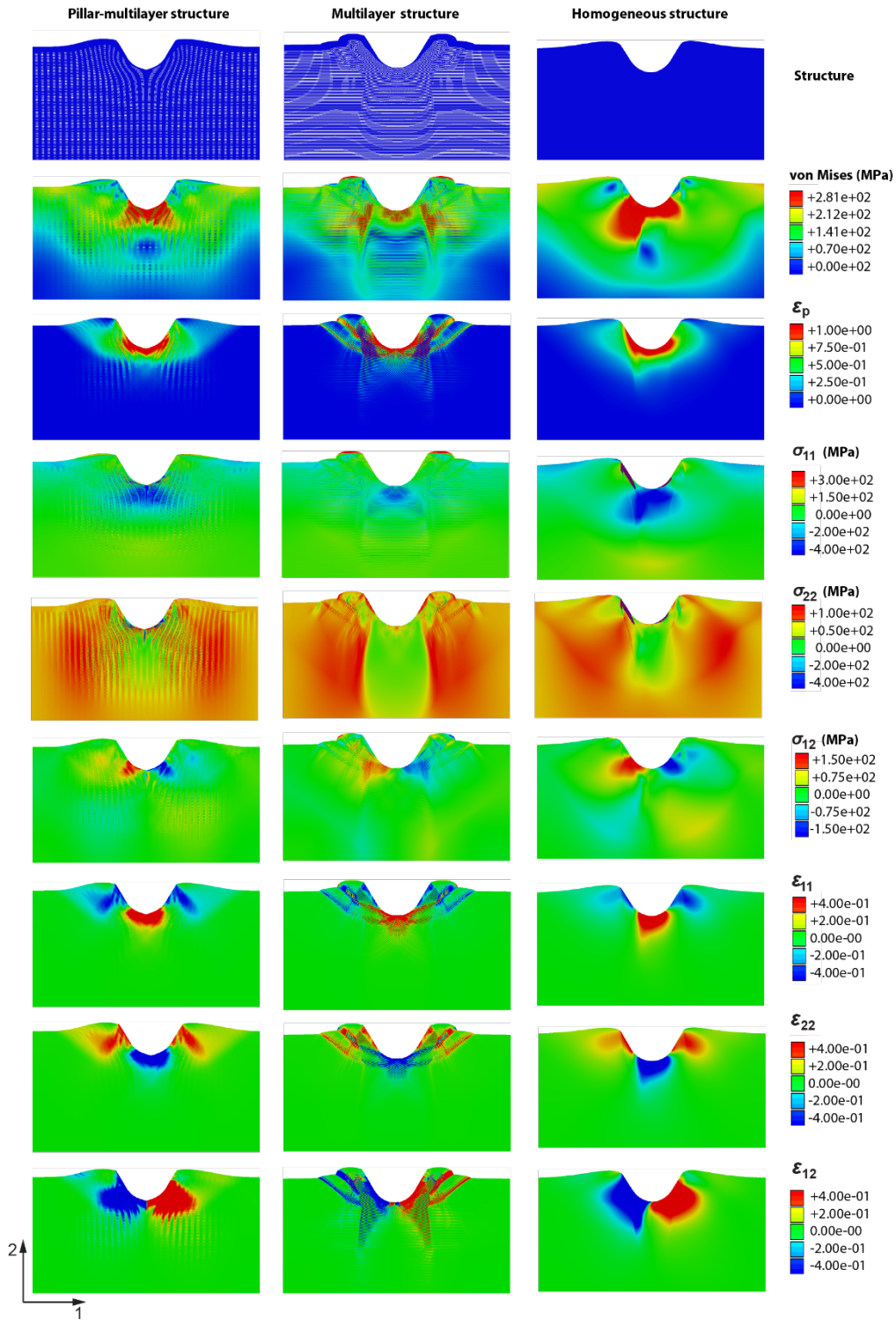
Fig. S11 | FEM simulation results: normal indentation after unloading. Three columns from left to right represent stress and strain distribution of the pillar-multilayer structure, multilayer structure, and a homogeneous material composed of the stiffer phase, respectively. Top to bottom rows represent structure, Mises stress, plastic strain (ε_p), normal stress (σ_{11} and σ_{22}), shear stress (σ_{12}), normal strain (ε_{11} and ε_{22}), and shear strain (ε_{12}), respectively.

Fig. S12 | FEM simulation results: inclined indentation at maximum load. Three columns from left to right represent stress and strain distribution of the pillar-multilayer structure, multilayer structure, and a homogeneous material composed of the stiffer phase, respectively. Top to bottom rows represent structure, Mises stress, plastic strain (ε_p), normal stress (σ_{11} and σ_{22}), shear stress (σ_{12}), normal strain (ε_{11} and ε_{22}), and shear strain (ε_{12}), respectively.
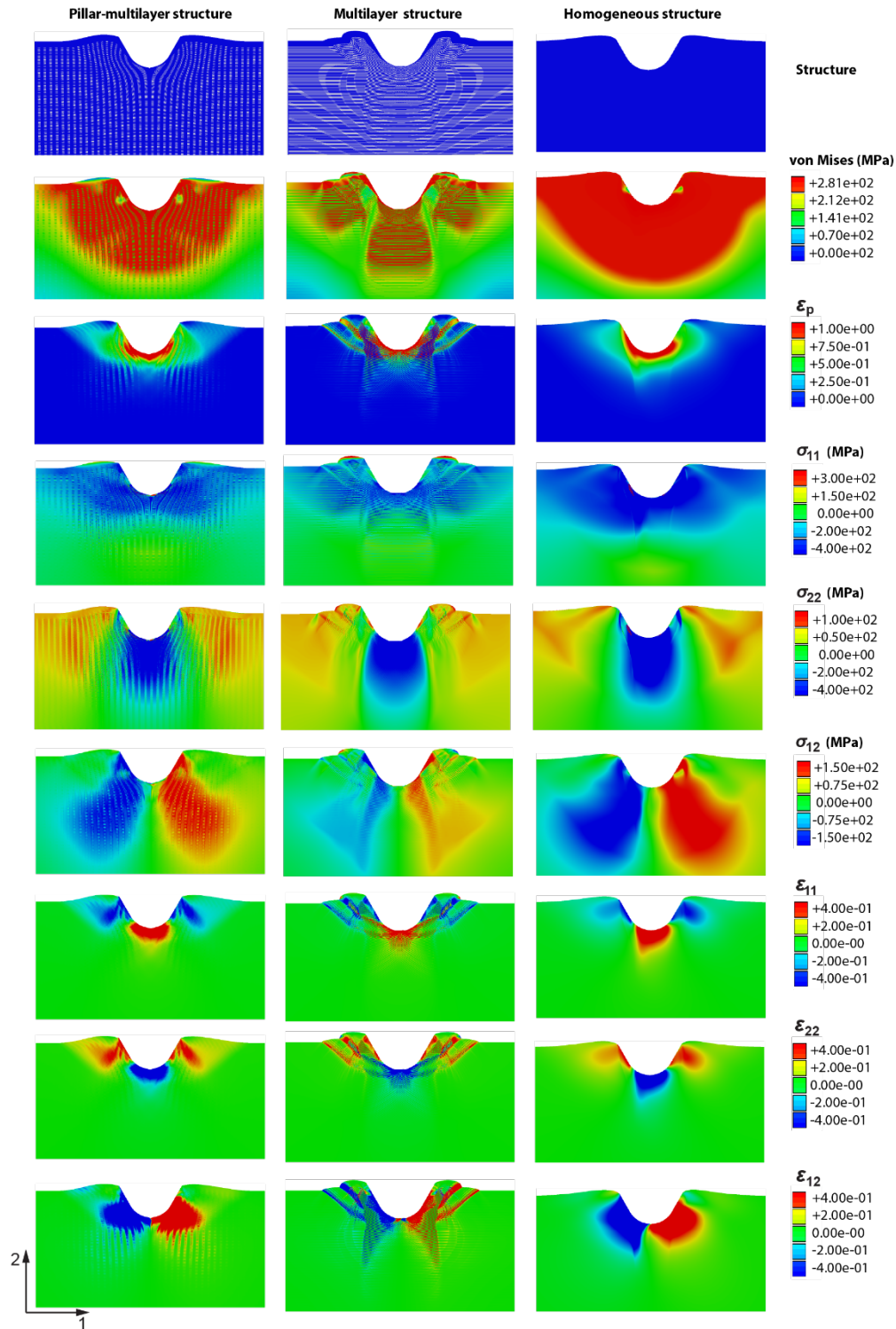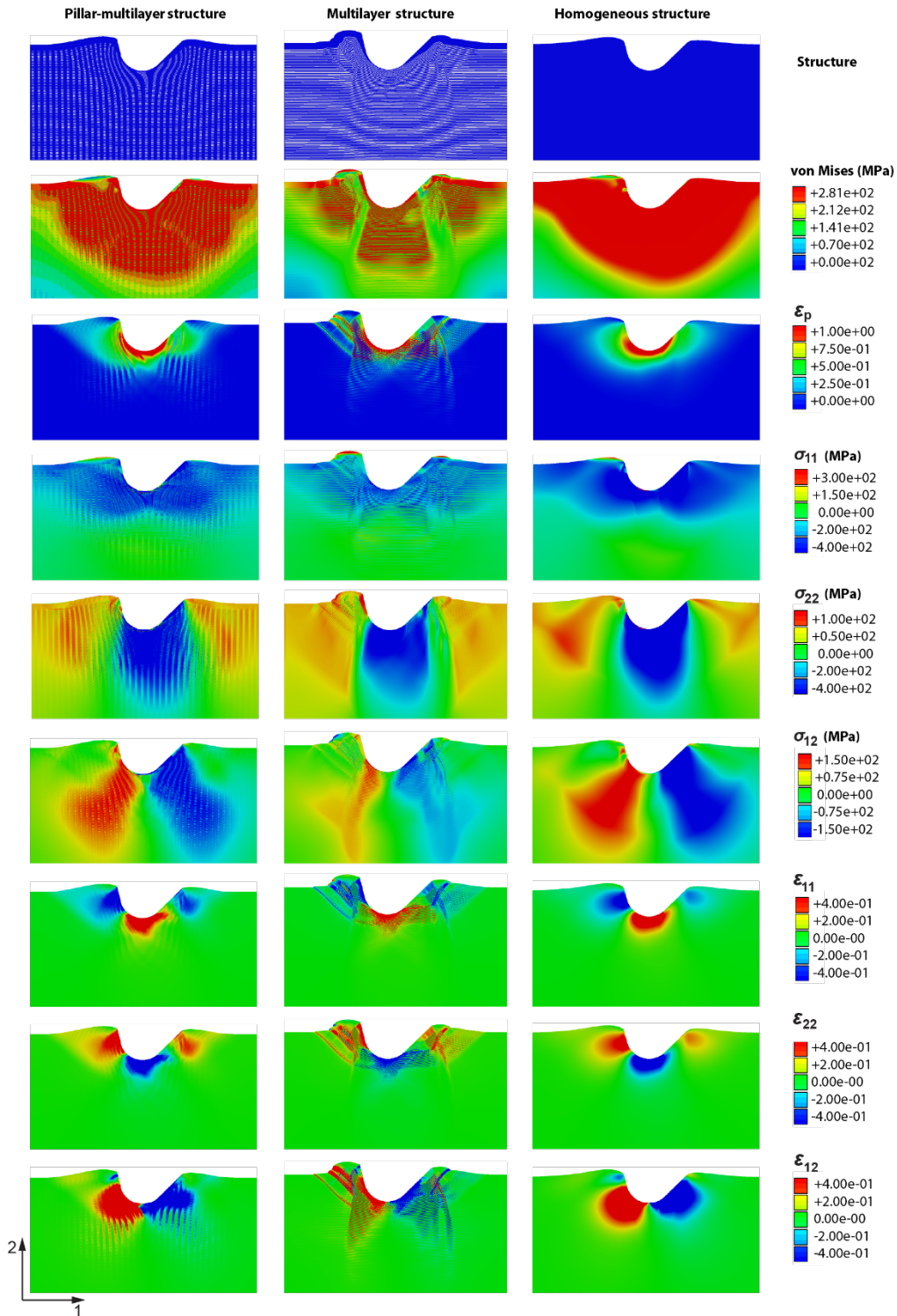
17
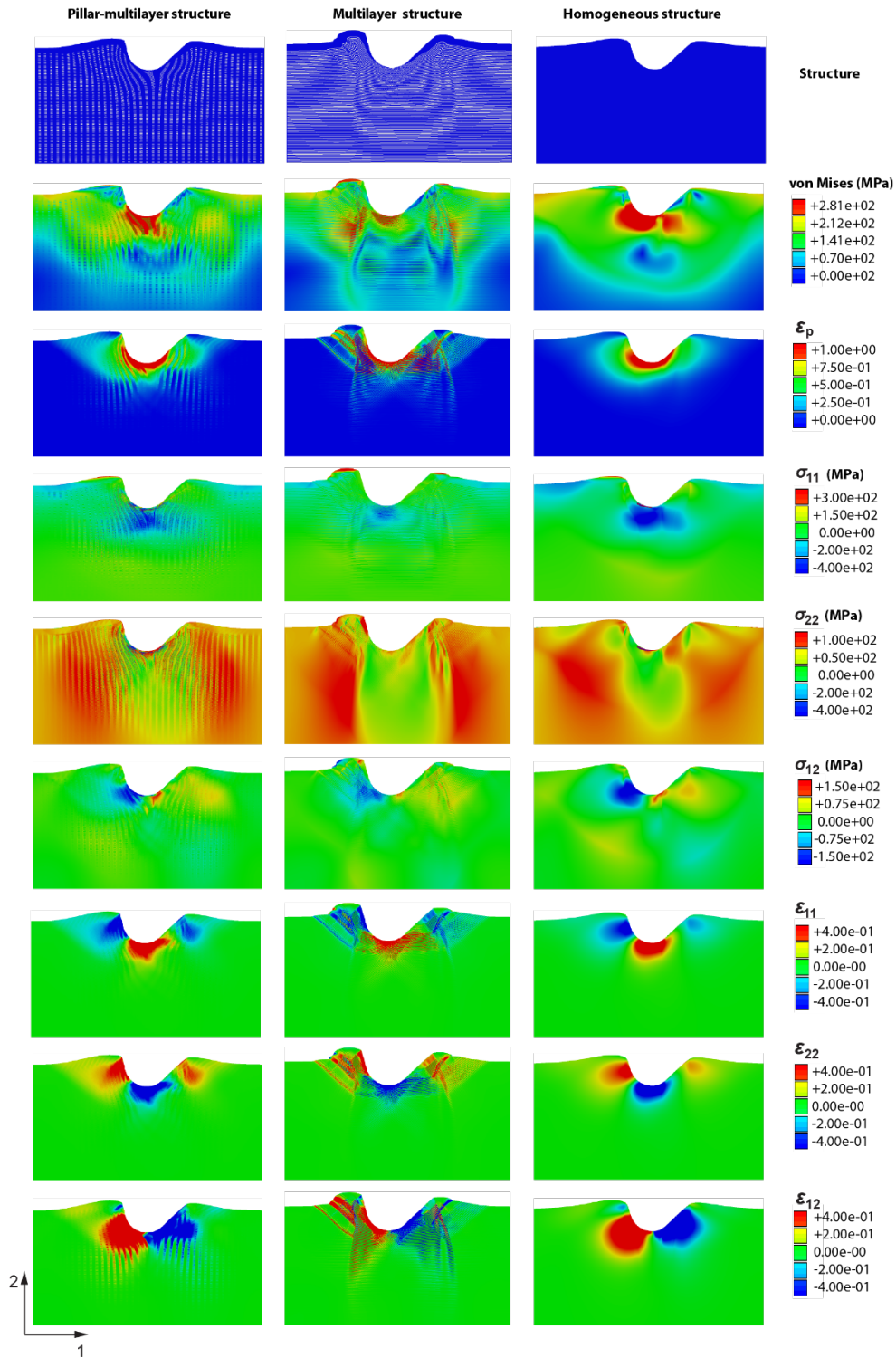
Fig. S13 | FEM simulation results: inclined indentation after unloading. Three columns from left to right represent stress and strain distribution of the pillar-multilayer structure, multilayer structure, and a homogeneous material composed of the stiffer phase, respectively. Top to bottom rows represent, structure, Mises stress, plastic strain (ε_p), normal stress (σ_{11} and σ_{22}), shear stress (σ_{12}), normal strain (ε_{11} and ε_{22}), and shear strain (ε_{12}), respectively.
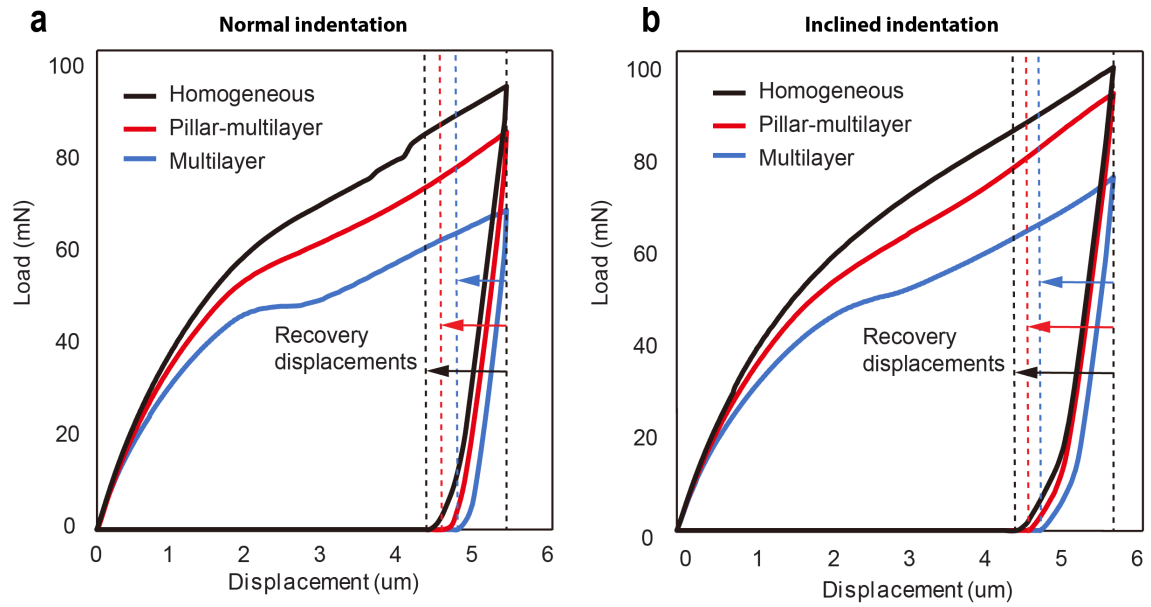
Fig. S14 | A comparison of the load-displacement curves for three different material microstructures under **a** normal and **b** inclined direction indentations from FEM simulation. The pillar-multilayer structure is stiffer, has higher yield stress and greater elastic recovery displacement (along the loading direction) than the multilayer structure without micro-pillars. The magnitudes of the elastic recovery displacements are marked by the arrows.
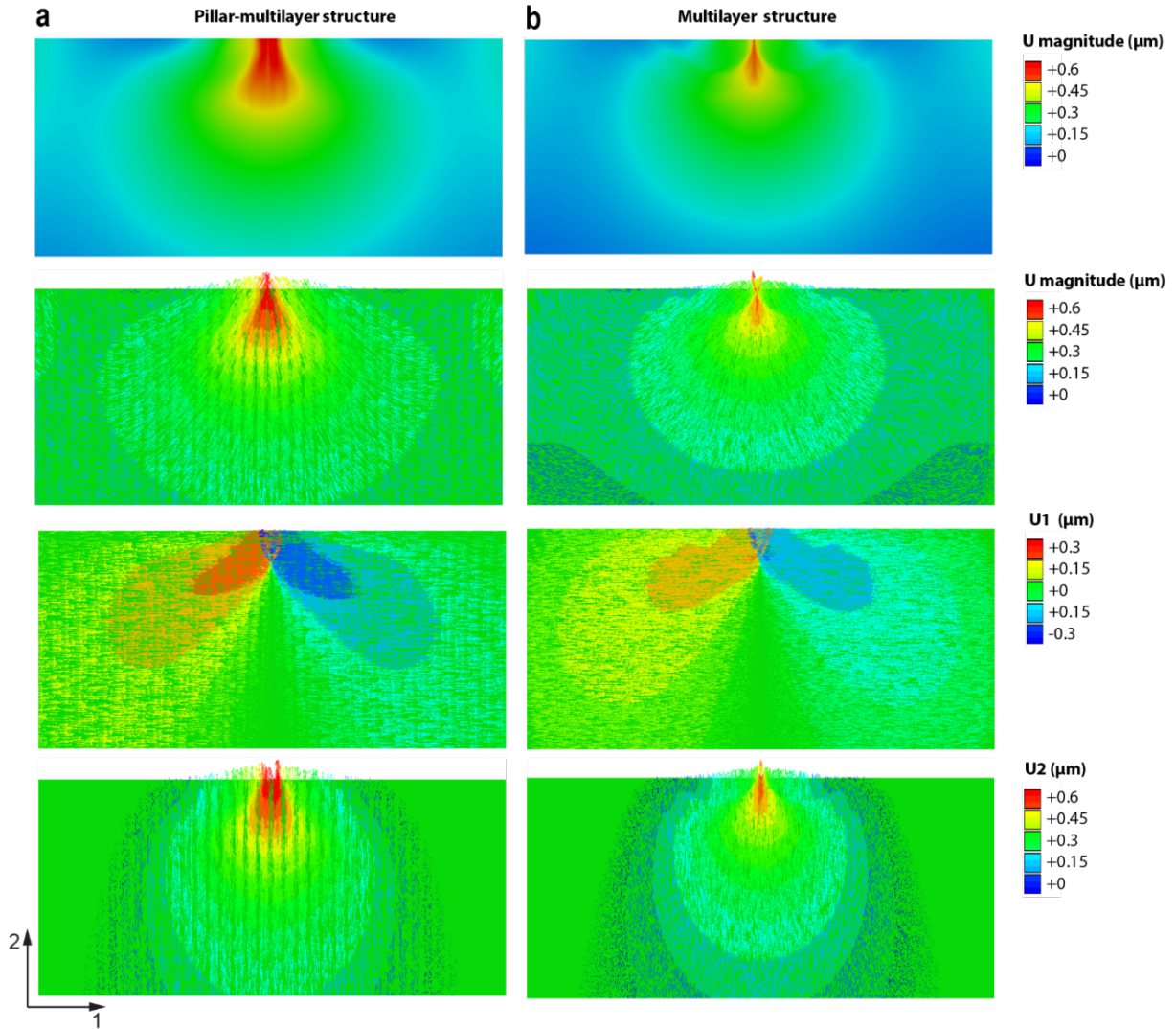
Fig. S15 | FEM simulation results: mapping of the recovery displacement from the maximum load status to the unloaded status. The displacement magnitude, vector, and the displacement components in directions 1 and 2 are mapped on the undeformed shape for **a** a pillar-multilayer structure in comparison to **b** a standard multilayer structure without micro-pillars.

Fig. S16 | Quantitative structural analysis of micro-pillars. a, Optical and **b**, SEM images of the in-plane polished samples for five beetle specimens with different colors, revealing the distribution of vertical micro-pillars. **c**, Binary graphs based on original SEM images. **d**, Nearest neighbor maps based on the analysis of binary graphs. **e**, Fast Fourier Transform graphs of binary graphs. **f**, Quantitative measurements of micro-pillars based on corresponding SEM images.

a

1 μm

b

Layer period distance

Average height (nm)

10

0

-10

-20

0   1   2   3   4

Distance, x (μm)

c

Autocorrelation period

Autocorrelation

0.8

0.4

0

-0.4

-0.8

-2   -1   0   1   2

Lag (μm)

d

Statistics of the layer period distance for yellow beetle

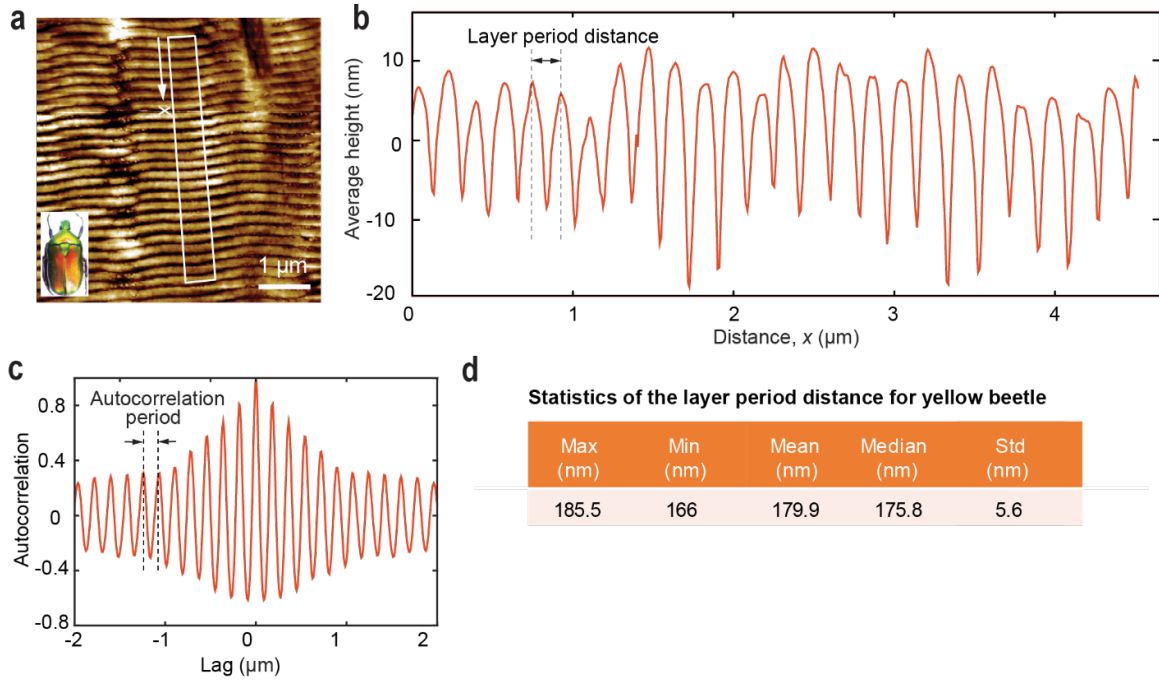| Max (nm)	Min (nm)	Mean (nm)	Median (nm)	Std (nm)
185.5	166	179.9	175.8	5.6

Fig. S17 | Evaluation of the layer period based on the atomic force microscopic images. a, An AFM image with the white rectangular showing the region used for the layer period analysis. **b**, The corresponding averaged height profile along the x direction marked in **a**. **c**, The layer distance is calculated by first performing an autocorrelation on the height profile shown in **b**, the peak positions of the autocorrelation is then analyzed to obtain the layer period as shown in **d**.
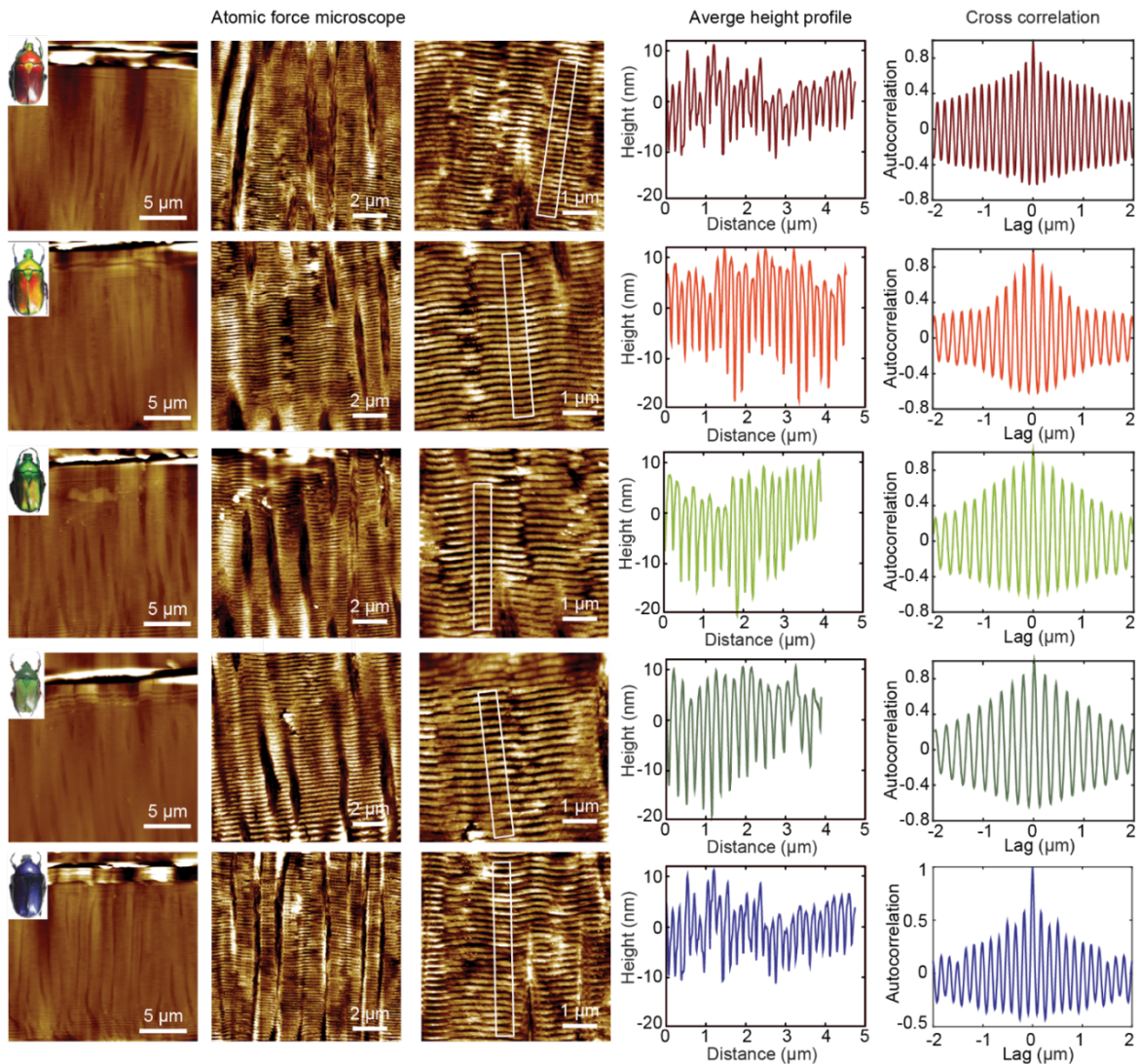
22

Fig. S18 | Evaluation of the layer period based on AFM measurements for beetles with five different colors. Plotted are the average height profiles and autocorrelation plots. The layer periods are calculated as the averaged peak to peak distances from the autocorrelation plots.
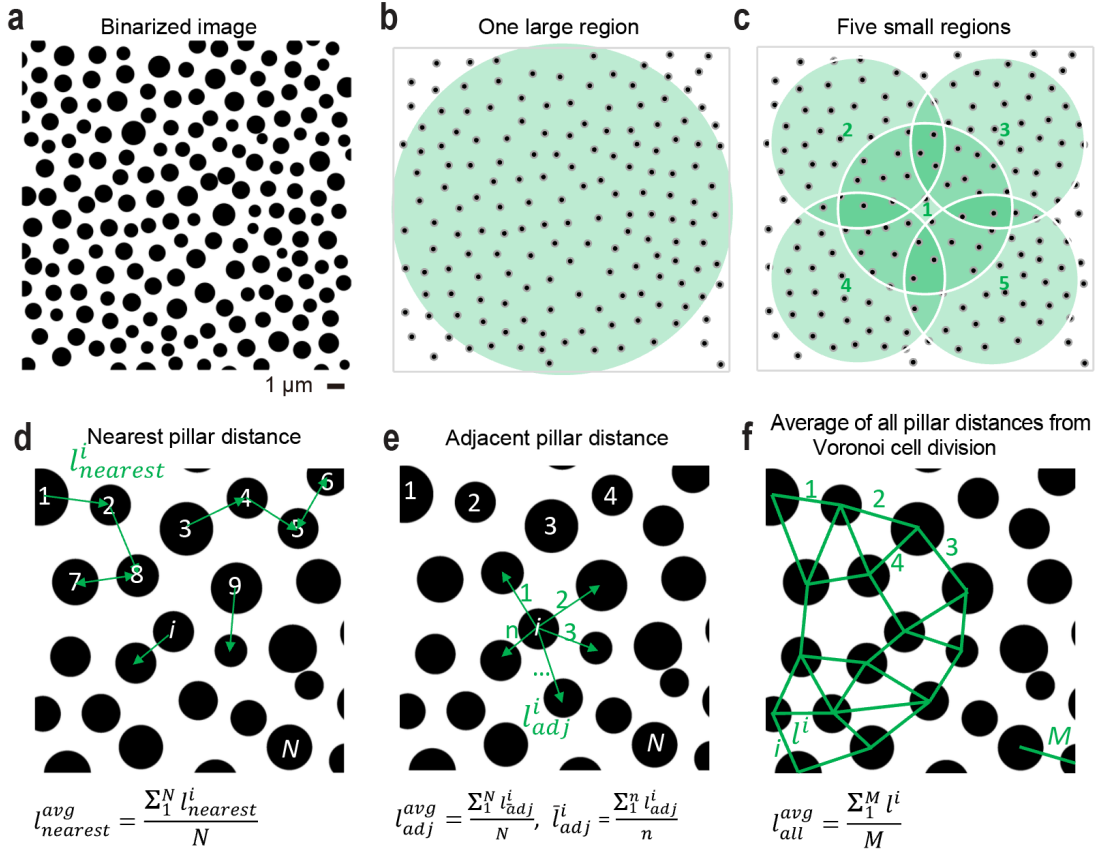
a Binarized image

b One large region

c Five small regions

1 μm

d Nearest pillar distance

$l^i_{nearest}$

$$l^{avg}_{nearest} = \frac{\Sigma^N_1 l^i_{nearest}}{N}$$

e Adjacent pillar distance

l^i_{adj}

$$l^{avg}_{adj} = \frac{\Sigma^N_1 l^i_{adj}}{N}, \quad \bar{l}^i_{adj} = \frac{\Sigma^n_1 l^i_{adj}}{n}$$

f Average of all pillar distances from Voronoi cell division

$$l^{avg}_{all} = \frac{\Sigma^M_1 l^i}{M}$$

Fig. S19 | Method to calculate the pillar distance. a, An example of the binarized image, where micro-pillars are fitted with circular disks. **b**, The circular area of interest to evaluate the pillar distance with a diameter of 19 μm. **c**, Five circular areas with a smaller diameter 9 μm are utilized to calculate the average diameters of multiple regions. **d-f**, Definition of the pillar distance with three methods: the nearest pillar distance, adjacent pillar distance, and average distance based on the Voronoi cell division method. The three different methods are used to characterize the nearest, local, and long-range characteristics of the pillar distance, respectively. Here, N is the total number of pillars, n is the number of neighbors of each pillar, M is the number of pillar distance from the Voronoi cell division method. Pillar distances of the five colored beetles are calculated by these three methods are summarized in Supplementary Figs. 20-25.
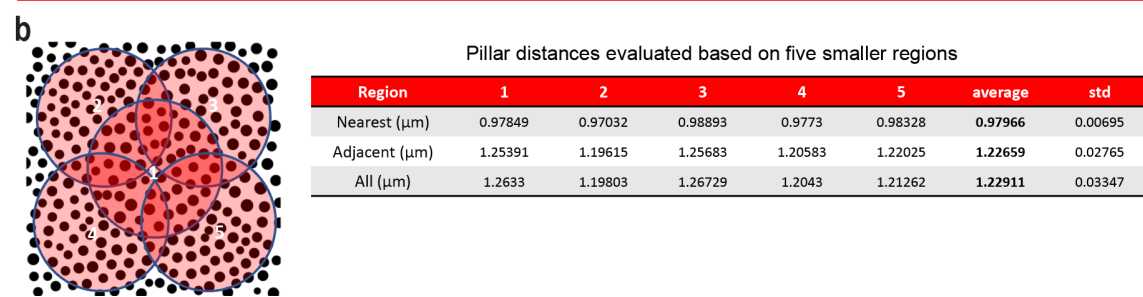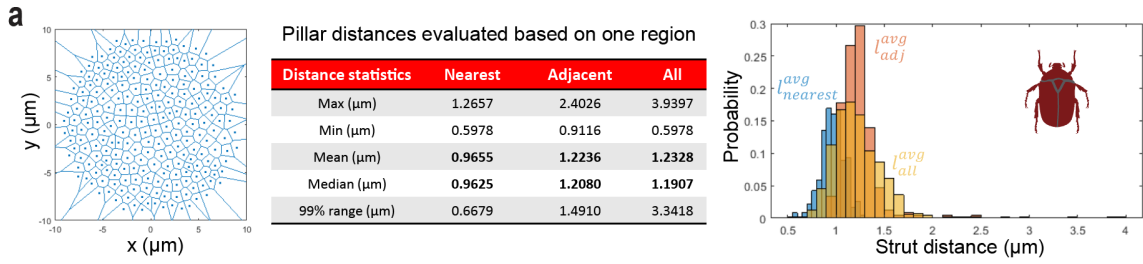
a

Pillar distances evaluated based on one region

Distance statistics	Nearest	Adjacent	All
Max (μm)	1.2657	2.4026	3.9397
Min (μm)	0.5978	0.9116	0.5978
Mean (μm)	**0.9655**	**1.2236**	**1.2328**
Median (μm)	**0.9625**	**1.2080**	**1.1907**
99% range (μm)	0.6679	1.4910	3.3418

b

Pillar distances evaluated based on five smaller regions

Region	1	2	3	4	5	average	std
Nearest (μm)	0.97849	0.97032	0.98893	0.9773	0.98328	**0.97966**	0.00695
Adjacent (μm)	1.25391	1.19615	1.25683	1.20583	1.22025	**1.22659**	0.02765
All (μm)	1.2633	1.19803	1.26729	1.2043	1.21262	**1.22911**	0.03347

Fig. S20 | Statistics of the pillar distance of the red beetle. Distances are evaluated on **a**, a large area with a diameter of 19 μm and **b**, five smaller areas based on the methods described in Supplementary Fig. 19.
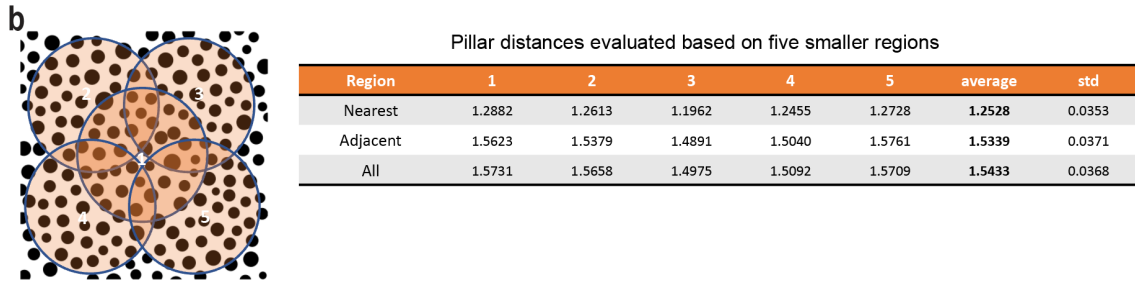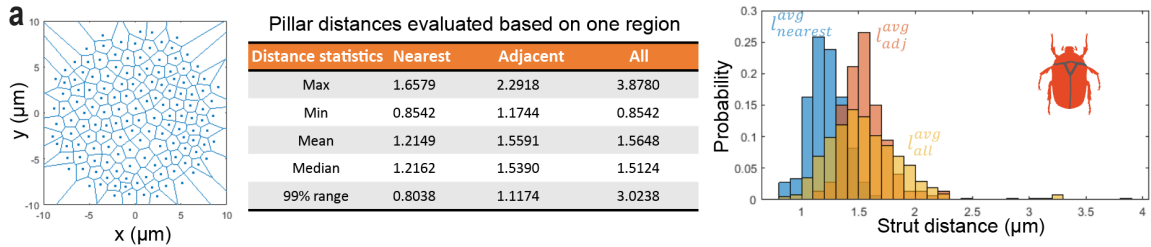
a

Pillar distances evaluated based on one region

Distance statistics	Nearest	Adjacent	All
Max	1.6579	2.2918	3.8780
Min	0.8542	1.1744	0.8542
Mean	1.2149	1.5591	1.5648
Median	1.2162	1.5390	1.5124
99% range	0.8038	1.1174	3.0238

b

Pillar distances evaluated based on five smaller regions

Region	1	2	3	4	5	average	std
Nearest	1.2882	1.2613	1.1962	1.2455	1.2728	**1.2528**	0.0353
Adjacent	1.5623	1.5379	1.4891	1.5040	1.5761	**1.5339**	0.0371
All	1.5731	1.5658	1.4975	1.5092	1.5709	**1.5433**	0.0368

Fig. S21 | Statistics of the pillar distance of the orange beetle. Distances are evaluated on **a**, a large area with a diameter of 19 μm and **b**, five smaller areas based on the methods described in Supplementary Fig. 19.
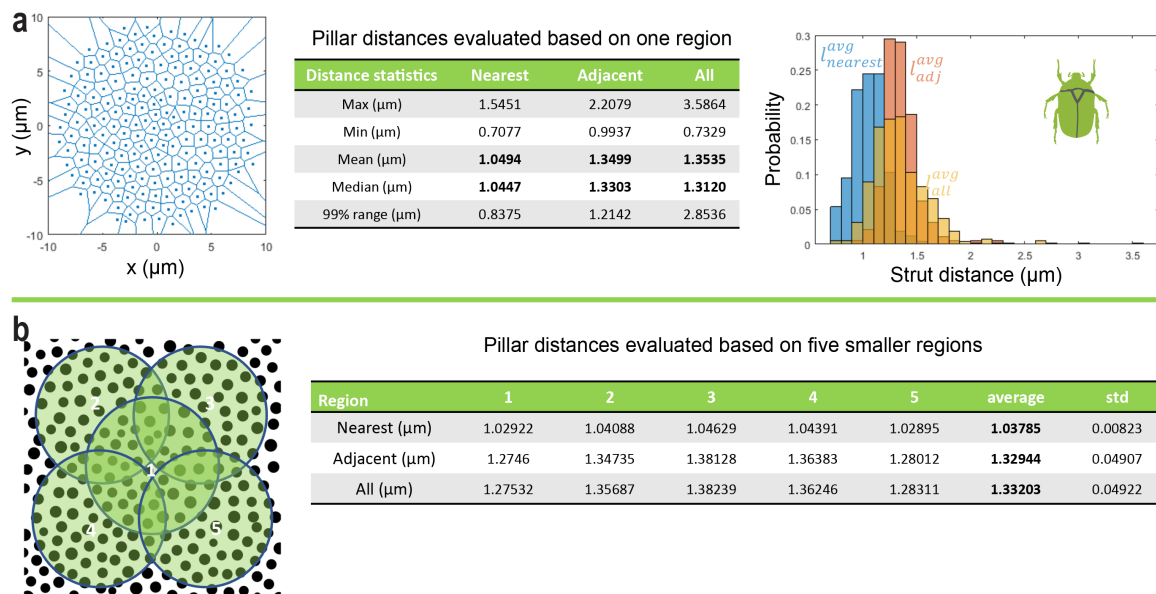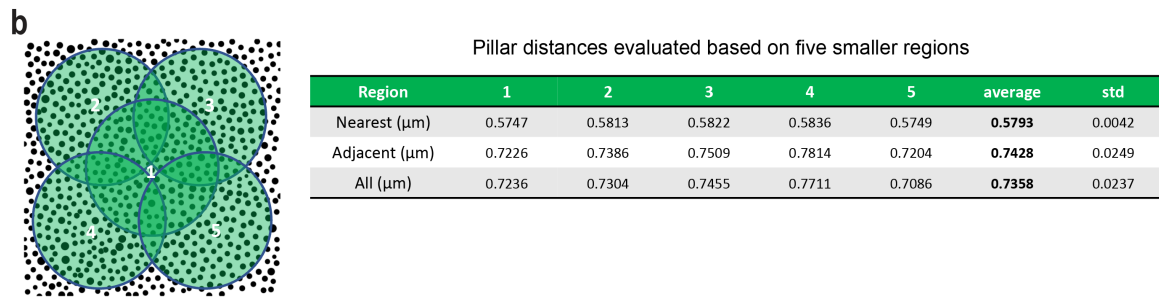
26

a

Pillar distances evaluated based on one region

Distance statistics	Nearest	Adjacent	All
Max (µm)	1.5451	2.2079	3.5864
Min (µm)	0.7077	0.9937	0.7329
Mean (µm)	**1.0494**	**1.3499**	**1.3535**
Median (µm)	**1.0447**	**1.3303**	**1.3120**
99% range (µm)	0.8375	1.2142	2.8536

b

Pillar distances evaluated based on five smaller regions

Region	1	2	3	4	5	average	std
Nearest (µm)	1.02922	1.04088	1.04629	1.04391	1.02895	**1.03785**	0.00823
Adjacent (µm)	1.2746	1.34735	1.38128	1.36383	1.28012	**1.32944**	0.04907
All (µm)	1.27532	1.35687	1.38239	1.36246	1.28311	**1.33203**	0.04922

Fig. S22 | Statistics of the pillar distance of the yellow-green beetle. Distances are evaluated on **a**, a large area with a diameter of 19 µm and **b**, five areas based on the methods described in Supplementary Fig. 19.
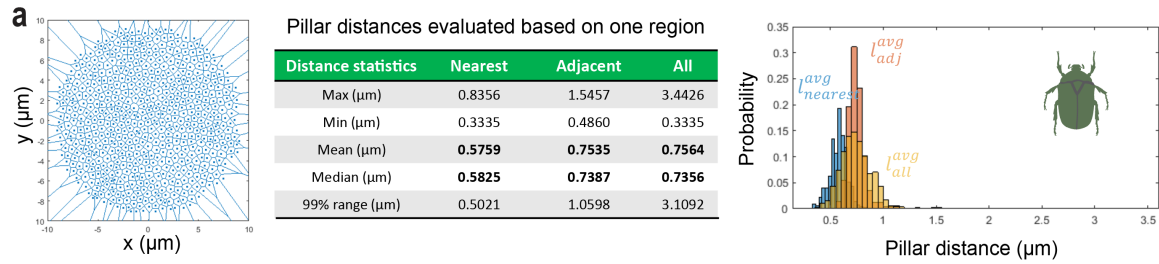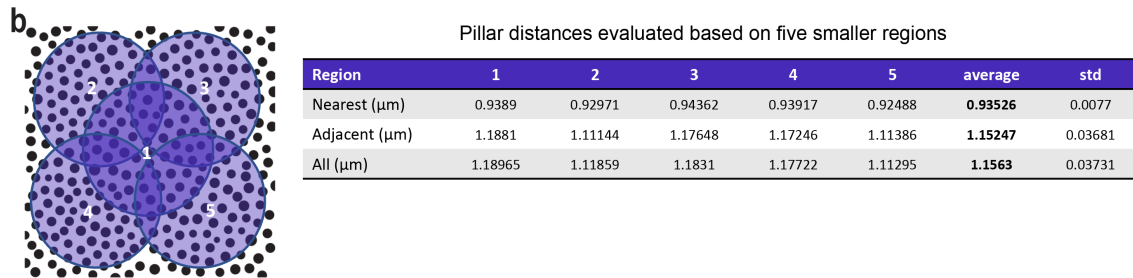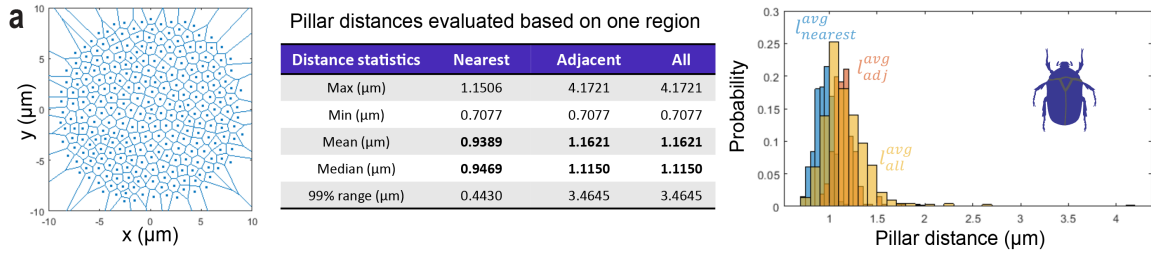
a

Pillar distances evaluated based on one region

Distance statistics	Nearest	Adjacent	All
Max (μm)	0.8356	1.5457	3.4426
Min (μm)	0.3335	0.4860	0.3335
Mean (μm)	**0.5759**	**0.7535**	**0.7564**
Median (μm)	**0.5825**	**0.7387**	**0.7356**
99% range (μm)	0.5021	1.0598	3.1092

b

Pillar distances evaluated based on five smaller regions

Region	1	2	3	4	5	average	std
Nearest (μm)	0.5747	0.5813	0.5822	0.5836	0.5749	**0.5793**	0.0042
Adjacent (μm)	0.7226	0.7386	0.7509	0.7814	0.7204	**0.7428**	0.0249
All (μm)	0.7236	0.7304	0.7455	0.7711	0.7086	**0.7358**	0.0237

Fig. S23 | Statistics of the pillar distance of the green beetle. Distances are evaluated on **a**, a large area with a diameter of 19 μm and **b**, five areas based on the methods described in Supplementary Fig. 19.

a Pillar distances evaluated based on one region

Distance statistics	Nearest	Adjacent	All
Max (μm)	1.1506	4.1721	4.1721
Min (μm)	0.7077	0.7077	0.7077
Mean (μm)	**0.9389**	**1.1621**	**1.1621**
Median (μm)	**0.9469**	**1.1150**	**1.1150**
99% range (μm)	0.4430	3.4645	3.4645

b Pillar distances evaluated based on five smaller regions

Region	1	2	3	4	5	average	std
Nearest (μm)	0.9389	0.92971	0.94362	0.93917	0.92488	**0.93526**	0.0077
Adjacent (μm)	1.1881	1.11144	1.17648	1.17246	1.11386	**1.15247**	0.03681
All (μm)	1.18965	1.11859	1.1831	1.17722	1.11295	**1.1563**	0.03731

Fig. S24 | Statistics of the pillar distance of the deep blue beetle. Distances are evaluated on **a**, a large area with a diameter of 19 μm and **b**, five areas based on the methods described in Supplementary Fig. 19.
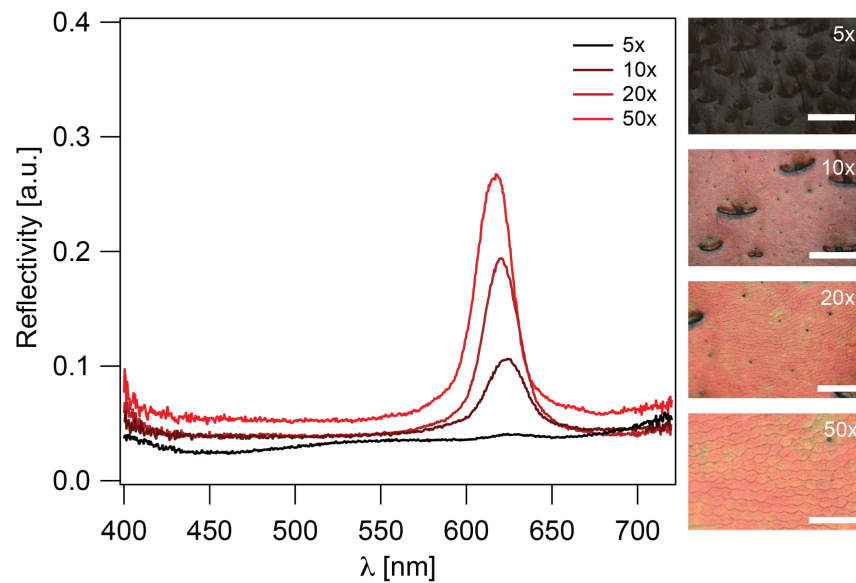
Fig. S25 | Change in color strength as a function of microscope objective collection angle. Reflection spectra of a beetle cuticle surface obtained through collection of light with different objectives of increasing collection angle. The photographs on the right correspond to the spectra shown on the left acquired with a 5×, 10×, 20×, and 50× objective. Scale bars from top to bottom: 1 mm, 500 μm, 200 μm, 100 μm.
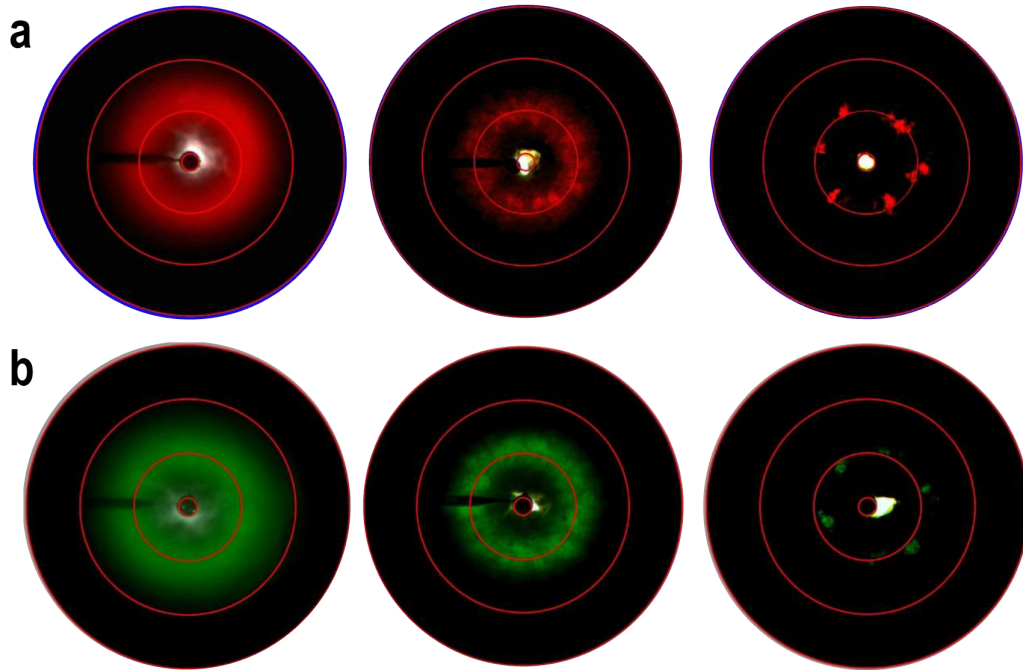
Fig. S26 | Diffraction images for (a) red beetle and (b) green beetle. The diffraction images in the first, second, third columns are collected using an imaging scatterometer with illumination spots of diameter varying from 200 µm to 5 µm, respectively. The red concentric circles from inside to outside represent θ = 5°, 30°, 60°, and 90°, respectively, for all images. Quasi-hexagonal diffraction patterns are only observed when illuminating a small area, indicating the short-range-order of the micro-pillars.
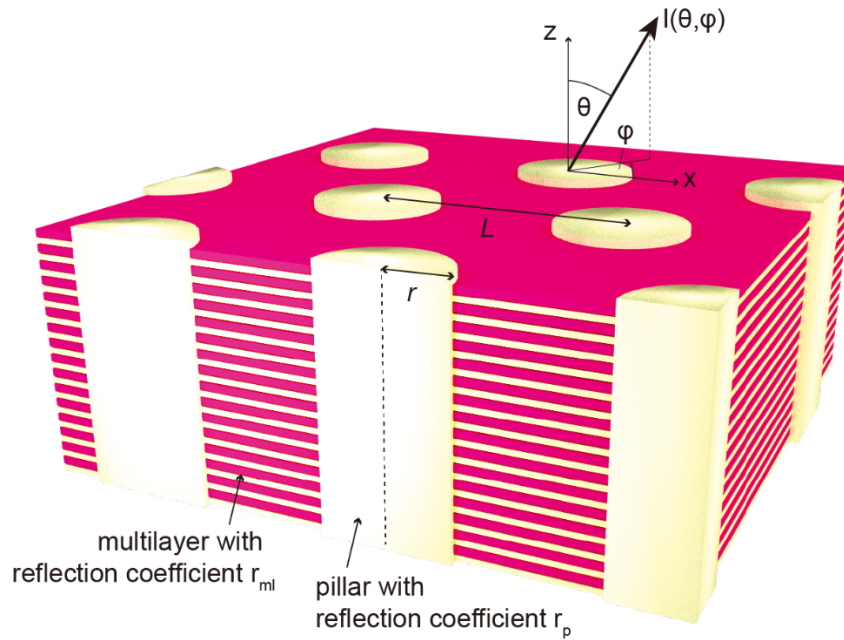
Fig. S27 | The beetles' photonic structure. Micro-pillars of radius r are arranged in a hexagonal array with lattice constant L. The reflection coefficients of the multilayer and pillar regions are r_{ml} and r_p, respectively. The reflected intensity $I(\theta, \varphi)$ is a function of the polar angle θ and the azimuthal angle φ.
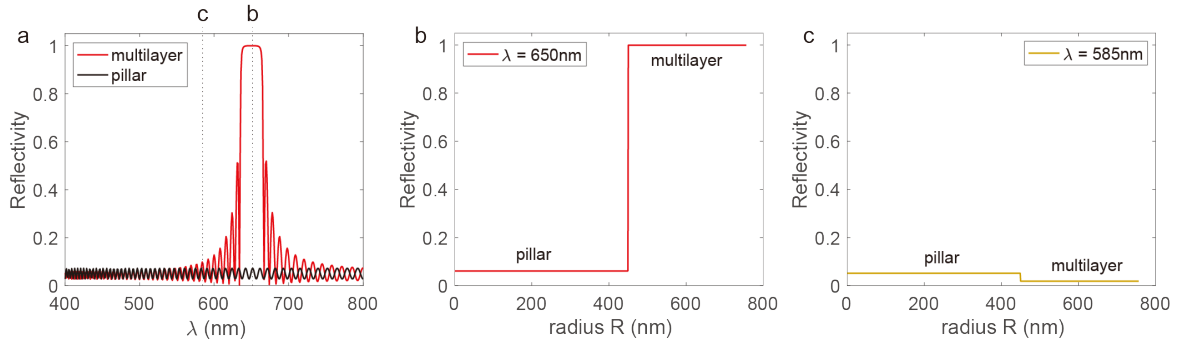
Fig. S28 | The unit cell's spectral and spatial reflectivity. a, Reflectivity spectra of multilayer and pillar regions. **b**, **c**, Reflectivity as a function of radial distance from the center of a pillar for λ = 650 nm (**b**) and λ = 585 nm (**c**).
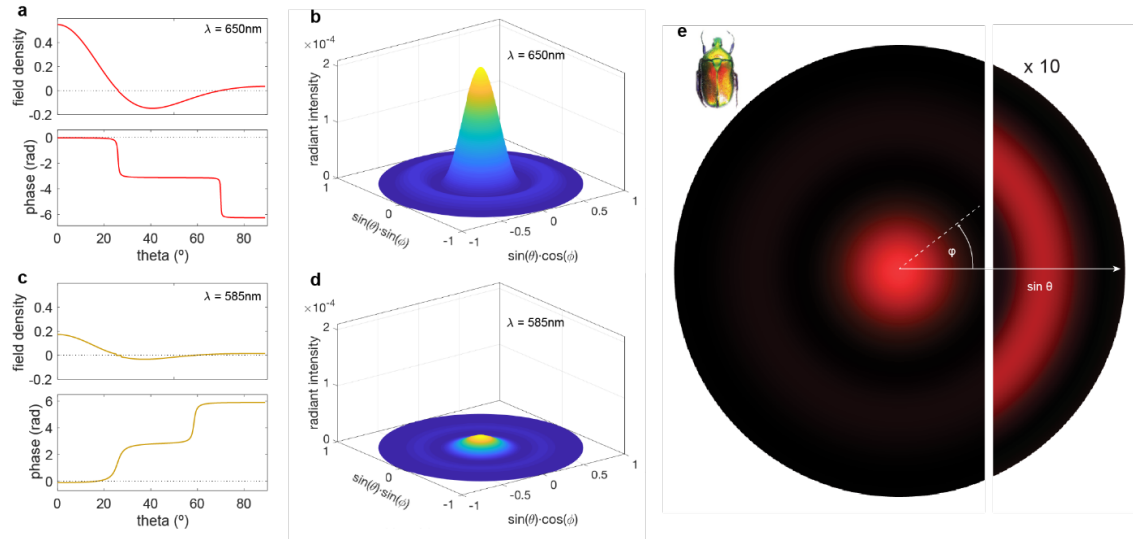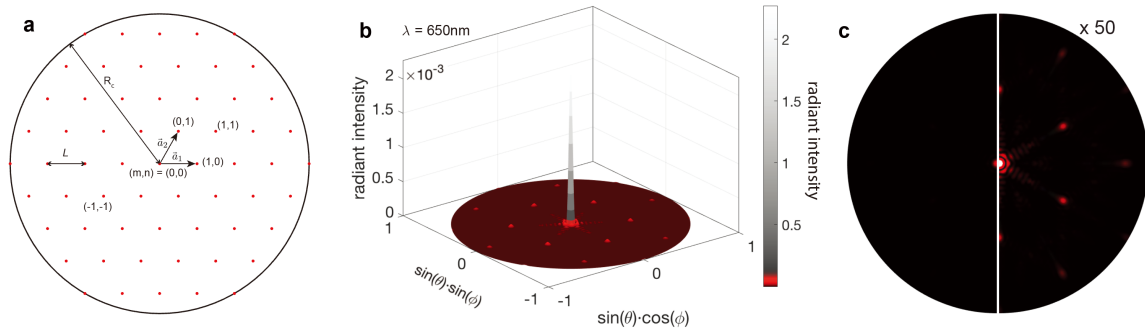
Fig. S29 | Angular diffraction signature of a single unit cell of a beetle with a multilayer peak reflection wavelength of 650 nm, a pillar radius $r = 450$ nm, and an inter-pillar distance of $L = 1512$ nm for normal light incidence. **a**, Field density and phase as a function of polar angle θ at $\lambda = 650$ nm. **b**, Radiant intensity as a function of observation direction at $\lambda = 650$nm. **c**, **d**, Same as **a** and **b** for $\lambda = 585$ nm. **e**, Color reflected by the beetle's structure as a function of angular direction.

Fig. S30 | Angular diffraction signature of a multilayer-pillar array of a beetle with a multilayer peak reflection wavelength of 650nm, a pillar radius $r = 450$ nm, and an inter-pillar distance of $L = 1512$ nm for normal light incidence. **a**, Location of unit cell centers on a hexagonal grid with lattice constant L within the coherence area of sunlight with radius $R_c = 10$ µm. The unit cell vectors are $\vec{a}_1 = \begin{pmatrix} 1 \\ 0 \end{pmatrix}$ and $\vec{a}_2 = \begin{pmatrix} 1/2 \\ \sqrt{3}/2 \end{pmatrix}$. **b**, Radiant intensity as a function of observation direction at $\lambda = 650$ nm. **c**, Color reflected by the beetle's structure as a function of angular direction. The left side represents the color intensities resulting from the conversion of angular radiant intensity normalized to the multilayers reflectivity values of $|r_{ml}(\lambda)|^2$; the right side is amplified by a factor of 50.
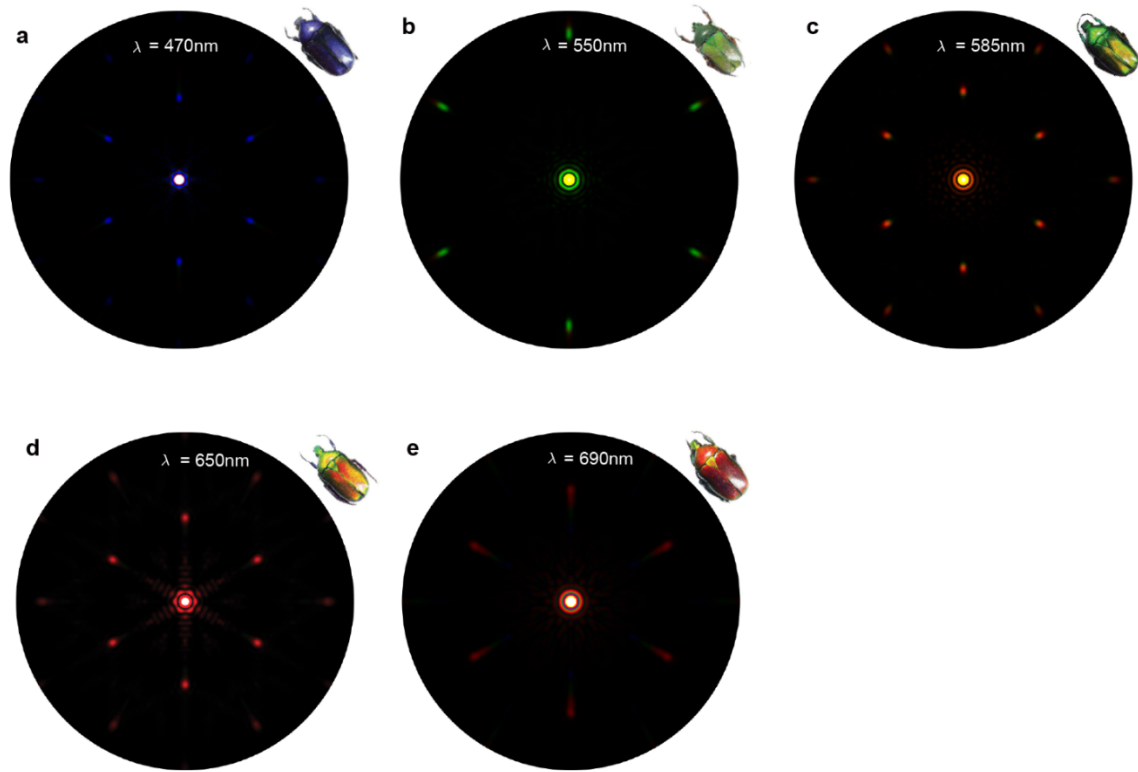
Fig. S31 | Modeled diffraction signatures for beetles with different colors. The multilayer reflection peak center wavelengths λ, pillar radius r, and inter-pillar distances L are **a**, $\lambda = 467$ nm, $r = 340$nm, $L = 1115$ nm; **b**, $\lambda = 549$ nm, $r = 220$ nm, $L= 736$ nm; **c**, $\lambda = 586$nm, r = 380 nm, L = 1312 nm; **d**, $\lambda = 645$nm, $r = 450$ nm, $L = 1512$ nm; and **e**, $\lambda = 690$ nm, $r = 360$nm, L=1191 nm. The color intensities are amplified by a factor of 50 from the original ones resulting from conversion of angular radiant intensity normalized to amount to the multilayer's reflectivity values of $|r_{ml}(\lambda)|^2$ to emphasize diffraction peaks.
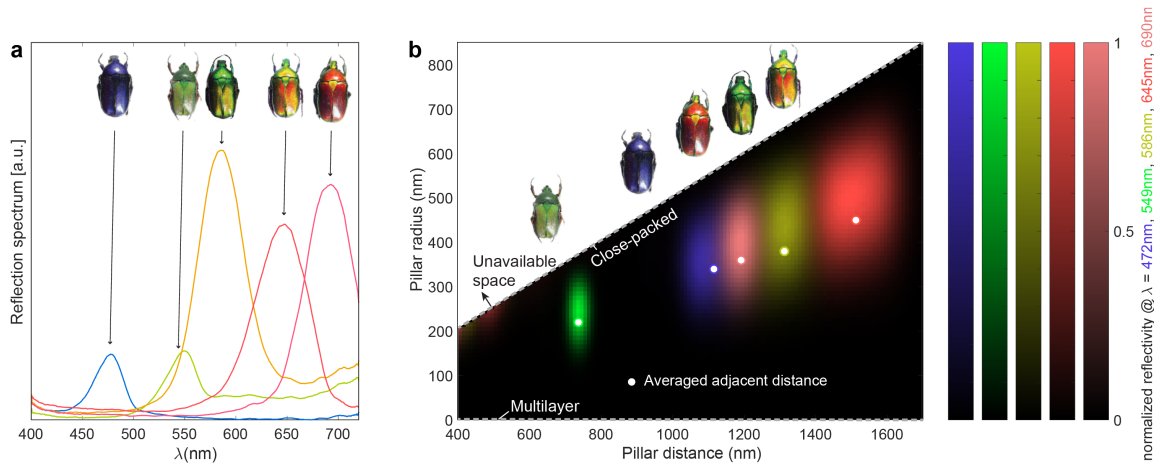
Fig. S32 | Measured spectra and comparison of the beetles' structural parameters with model predictions. a, Measured reflection spectra of five beetles. Spectra are given in arbitrary units as measurements were conducted with a micro-spectrometric setup collecting light through a 50× objective of an Olympus microscope with a limited numerical aperture of 0.5; this allows to get a good estimate of the spectral composition of light reflected from the beetle's pillar-multilayer architectures; it does not ensure that all reflected light is captured therefore not allowing to obtain reliable estimates on the absolute intensity (for that a measurement with an integrating sphere would be more appropriate). **b**, Strength of diffraction in the first diffraction order located at $\theta = \sin^{-1}(\lambda/L)$ modeled for varying pillar distances and radii for the multilayer architectures of the five beetles shown in **a**. The white circles mark the median pillar distances and radii measured for the five different beetles.
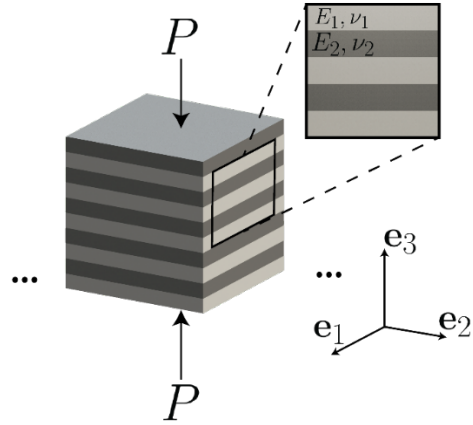
Fig. S33 | The two-phases multilayer model used in mechanical modeling. A simple laminate, with an even number of interfaces (or a very large number of interfaces) in the e_3 direction and infinitely large layers along the $e_1 \cdot e_2$ plane.
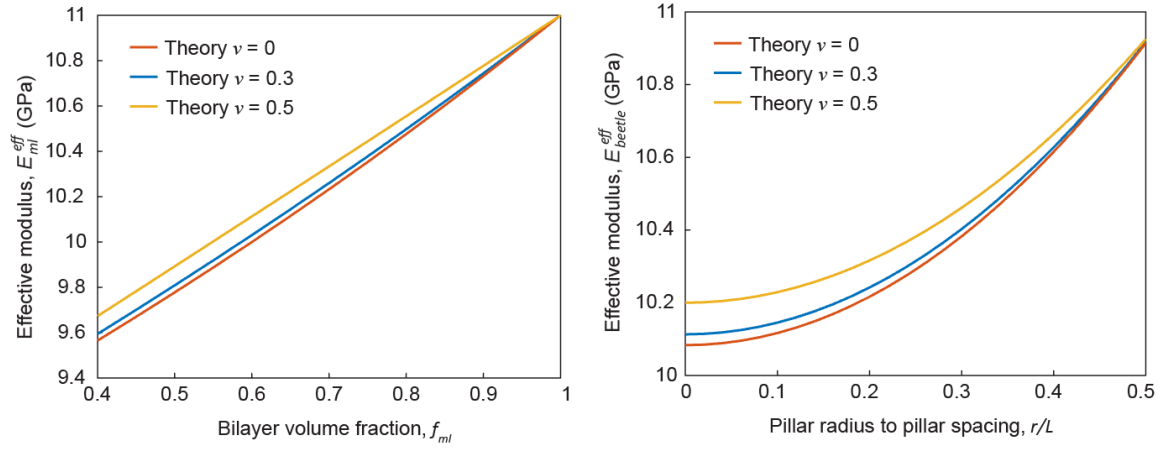
Fig. S34 | Mechanical modeling results of the effective modulus. Effective modulus of **a**, the multilayer structure and **b**, the micropillar reinforced multilayer structure of beetle's cuticle. Results are plotted for Poisson's ratios of $v = 0$, 0.3, and 0.5.
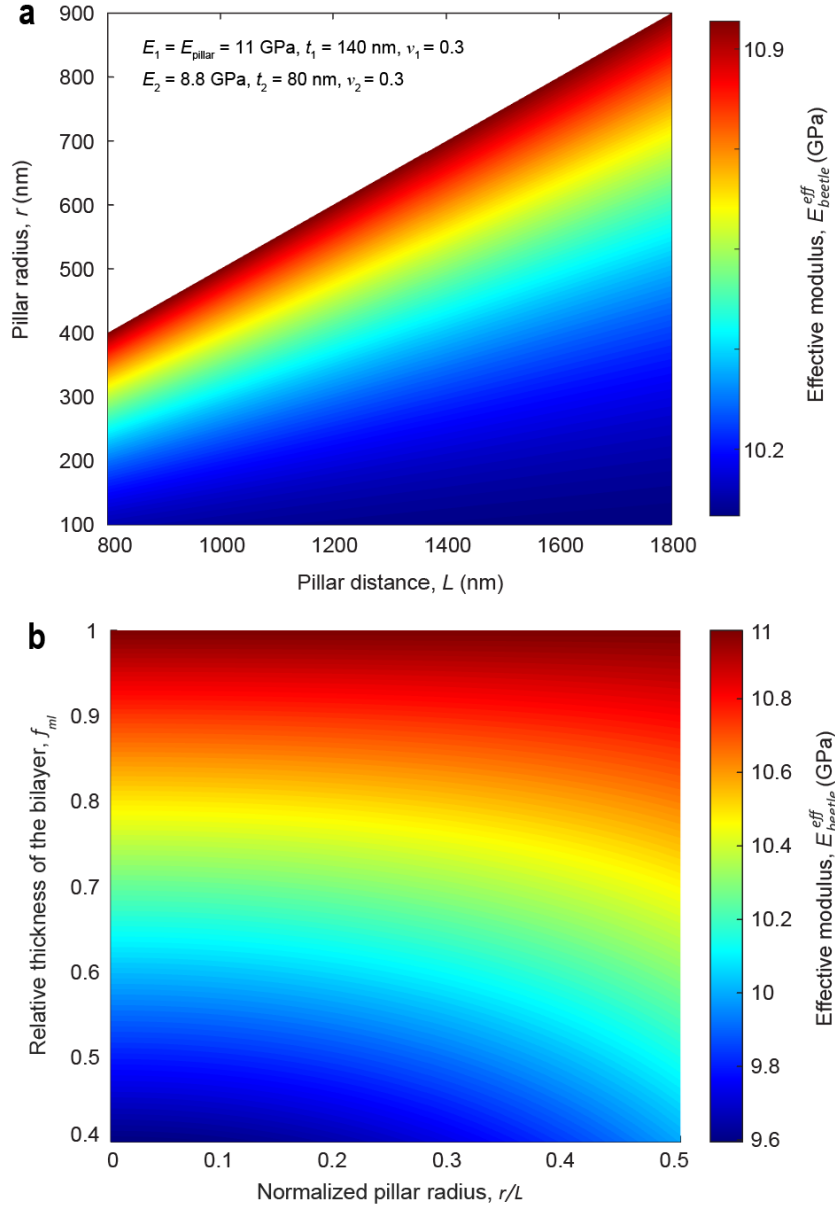
Fig. S35 | Mechanical modeling results. a, Contour plot showing the dependency of effective stiffness on the pillar radius and pillar distance for the micropillar-multilayer structure. The white region in the plot occurs when the pillar radius and distance are geometrically incompatible based on a hexagonal pillar arrangement. **b**, The dependency of effective stiffness on the multilayer spacing ratio f_{ml} and pillar to radius distance ratio r/L.
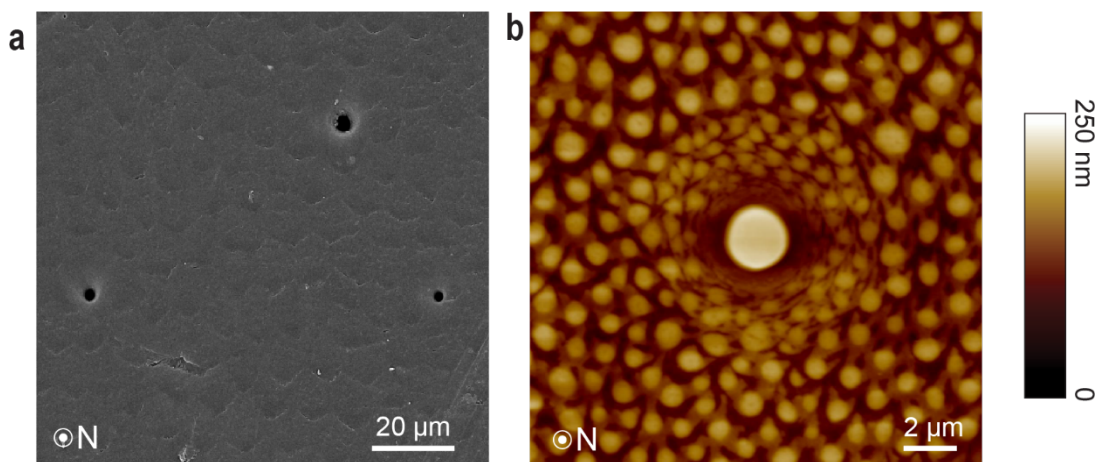
Fig. S36 | Microstructural features in the vicinity of a gland cell pore. a, A top-view SEM image of a cuticle surface, showing three pore conductors. **b**, AFM height image acquired on an in-plane polished sample that shows the reduced radius and increased density of micro-pillars close to a gland cell pore.
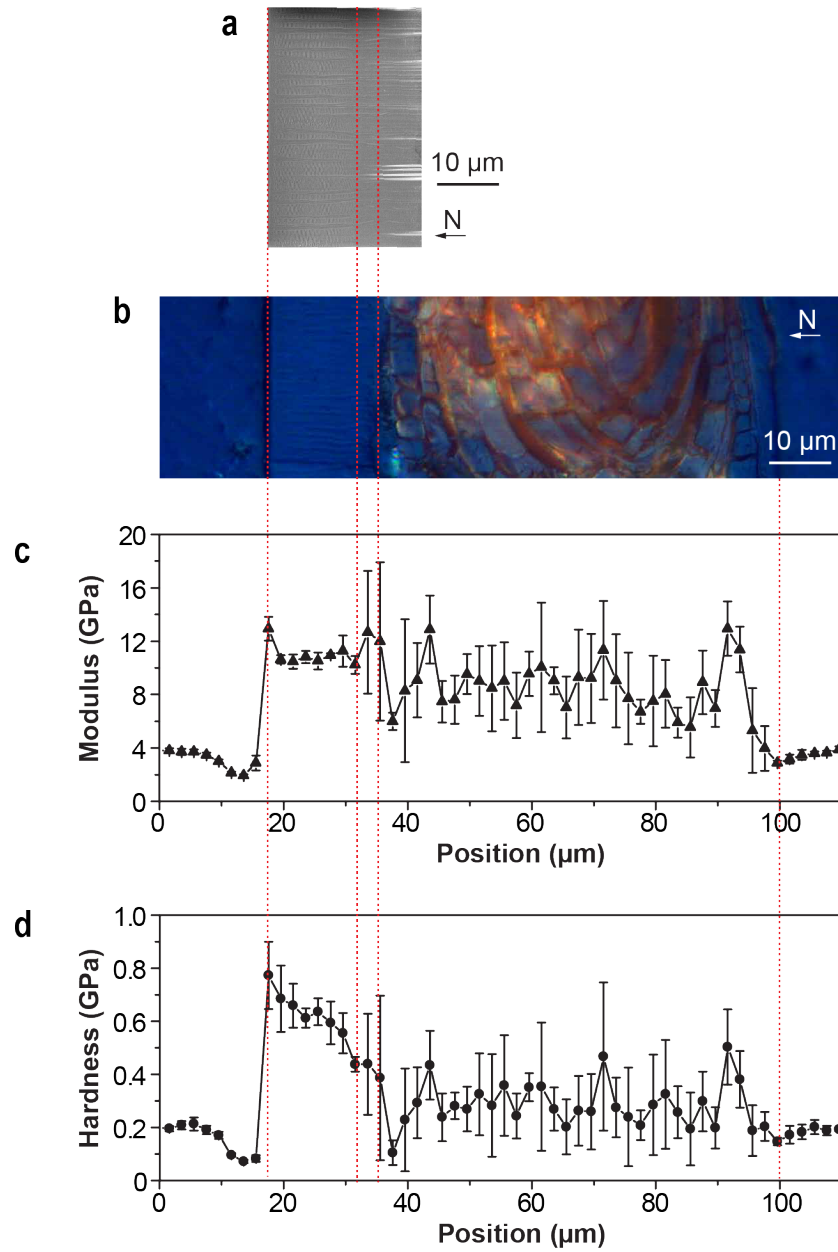
Fig. S37 | Measurement of mechanical properties based on nanoindentation mapping across the entire cross-section of the elytra cuticle. a, SEM image of the photonic region after FIB milling along the vertical cross-sectional direction. **b**, Optical image of the entire cross-section of the elytra cuticle after polishing. **c**, Averaged indentation modulus and hardness based on Oliver-Pharr analysis as a function of distance across the entire cross-section. The vertical error bars represent the standard deviation.

SI References

1. Born, M. & Wolf, E. Principles of optics: electromagnetic theory of propagation, interference and diffraction of light. (Elsevier, 2013).
2. Willis, J. Mechanics of composites. (Ecole polytechnique, 2002).